2004-08-13

An Examination into the Statistics of the Singular Vectors for the Multi-User MIMO Wireless Channel

Scott Nathan Gunyan
Brigham Young University - Provo

BYU ScholarsArchive Citation
Gunyan, Scott Nathan, "An Examination into the Statistics of the Singular Vectors for the Multi-User MIMO Wireless Channel" (2004). *Theses and Dissertations*. 179.
https://scholarsarchive.byu.edu/etd/179

AN EXAMINATION INTO THE STATISTICS OF THE SINGULAR VECTORS FOR THE MULTI-USER MIMO WIRELESS CHANNEL

by

Scott N. Gunyan

A thesis submitted to the faculty of

Brigham Young University

in partial fulfillment of the requirements for the degree of

Master of Science

Department of Electrical and Computer Engineering

Brigham Young University

December 2004

BRIGHAM YOUNG UNIVERSITY

GRADUATE COMMITTEE APPROVAL

of a thesis submitted by

Scott N. Gunyan

This thesis has been read by each member of the following graduate committee and by majority vote has been found to be satisfactory.

Date	Michael A. Jensen, Chair
Date	A. Lee Swindlehurst
Date	Brian D. Jeffs

BRIGHAM YOUNG UNIVERSITY

As chair of the candidate's graduate committee, I have read the thesis of Scott N. Gunyan in its final form and have found that (1) its format, citations, and bibliographical style are consistent and acceptable and fulfill university and department style requirements; (2) its illustrative materials including figures, tables, and charts are in place; and (3) the final manuscript is satisfactory to the graduate committee and is ready for submission to the university library.

Date

Michael A. Jensen
Chair, Graduate Committee

Accepted for the Department

Michael A. Jensen
Graduate Coordinator

Accepted for the College

Douglas M. Chabries
Dean, College of Engineering and Technology

ABSTRACT

AN EXAMINATION INTO THE STATISTICS OF THE SINGULAR VECTORS FOR THE MULTI-USER MIMO WIRELESS CHANNEL

Scott N. Gunyan

Department of Electrical and Computer Engineering

Master of Science

Many capacity and near-capacity achieving methods in multiple-input-multiple-output (MIMO) wireless channels make use of the singular value decomposition (SVD) of the channel matrix. For the multi-user case, the SVD of the channel matrix for each user may result in right and left singular vectors that are similar between users. This proposes another descriptive characterization of the multi-user MIMO channel. Closely aligned singular vectors between any two users could reduce the achievable signaling rates of signal processing communication methods as one user would be more difficult to resolve in space-time from another. An examination into how this alignment can be described in realistic MIMO multipath channels using a two ring channel model is presented. The effects of correlation between singular vectors on achievable signaling rates is shown for one existing algorithm that approaches the sum capacity known as block-diagonalization. Analyzed is actual data collected in several indoor and outdoor experiments performed using newly constructed measurement hardware that extends the capabilities of an existing MIMO measurement system.

ACKNOWLEDGMENTS

To Dr. Jensen, for his confidence and support, providing me the opportunity to perform this work. To my wife, Marie, for her continued patience and underlying support in all I do. To Jon Wallace, for his extensive previous work that allowed much of the current work here, and his continuing collaboration. To the faculty at Brigham Young University for a wonderful and unsurpassed educational experience.

Contents

List of Tables

List of Figures

Chapter 1

Introduction

The explosive growth of wireless devices and their use in today's world is adding more and more competing users to allocated electromagnetic spectrum. These devices include cell phones, pagers, 802.11 standard networking hardware, satellite communications, and various aerospace and military applications, all of which are becoming more computationally powerful and complex. These technological and economical developments are compounded by the increased demand for new applications such as video and audio streaming and other digital data sharing which require higher signaling rates. This increased demand has generated increased interest in examining multi-user wireless channels and the achievable data rates given a fixed bandwidth. Accurate electromagnetic models of the multi-user wireless channel can help assess the performance of existing coding algorithms as well as provide realistic capacity limits in this search to increase information rate. If the model is intuitive and insightful as well, it could help in the development of new algorithms that exploit the parameters of the model in its use.

1.1 Background

Traditionally, time and frequency based processing has been employed to attempt to maximize system throughput on both single user (point to point) and multiuser applications. Using this perspective, multipath interference of electromagnetic signals are a detriment to wireless transmission due to reductions in signal to noise ratio (SNR). As a mobile subscriber moves through a multipath channel, the signal strength varies dramatically due to the interference of the multiple electromagnetic waves. This is described statistically as fast or Rayleigh fading, with typical fade depths of around 20dB. For the single-input-single-output (SISO) scheme, Shannon's ground breaking work initiating the area of information theory showed that channel capacity depends on the log of the SNR [1], so that multipath interference can reduce achievable transmission rates.

Recent developments in information theory, however, show that the use of multiple antenna arrays in multipath wireless channels allows for large increases in theoretical capacity over the SISO case. These multiple-input-multiple-output (MIMO) schemes allow for processing in the spatial dimension as well as the time and frequency based methods available to SISO transmission. With MIMO transmission, multipath in the wireless channel response can be exploited through space-time signal processing to provide up to an N-fold increase in capacity, where N is the smaller of the number of transmit or receive antennas [2]. Multipath effects have been examined extensively and viable outdoor [3], [4] and indoor [5], [6] statistical models have been developed focusing on ray based parameters such as angle of arrival, excess delay (delay spread), and ray clustering in both temporal and angular dimensions. Antenna correlation versus separation distance is another statistical parameter that has been researched [7], [8].

To date, much research on space-time signal processing has focused on the point-to-point MIMO scenario where a single user has full use of the allocated bandwidth (see, for example [9], [10]). More recently, attention has shifted to the multi-user MIMO case, where allocated bandwidth is shared between the co-channel users. Many of these methods employ the singular value decomposition (SVD) of the MIMO channel matrix to precode and decode the sent data streams. One such method considered in this thesis is known as block-diagonalization and is given in [11]. Because these methods use the SVD to achieve multi-user signaling, it is interesting to explore the behavior of the channel singular vectors in a multi-user channel. Due to recent emergence of these techniques, such a study has yet to be completed.

1.2 Contributions

This thesis investigates the properties of the two-user downlink MIMO wireless channel. The study uses two ring channel models to examine correlation in the singular vectors of the two users. Results from Monte Carlo simulations performed using these two ring models provide insight into how different scattering environments statistically effect the channels seen by different mobile users. Real data collected from a multi-user MIMO measurement system is also analyzed, and the results are compared to those from simulations. This coupled measurement and modeling campaign provides new insights into the behavior of multi-user MIMO wireless channels.

The effects of alignment in the multi-user singular vectors on achievable rates for the block-diagonalization algorithm are also explored. This algorithm applies to multi-user MIMO broadcast channels where the total number of receive antennas is less than or equal to the total number of transmit antennas employed. This provides a representation for how correlation in the singular vectors can effect theoretical capacity for the broadcast or multiple access channel case. Based on this study, inferences are drawn concerning how this correlation impacts capacity for the case where the total number of receive antennas is more than the total number of transmit antennas, as would be likely in channels with a large number of users or ad-hoc networks.

1.3 Organization of the Thesis

Chapter 2 introduces the Saleh-Valenzuela MIMO channel model [5] and then shows how its parameters can be cast into the two ring channel model. Here, notation used throughout the thesis is developed. This chapter also demonstrates how the SVD can be used to achieve multiple parallel bit streams by means of a simple example. The chapter ends with a mathematical description of correlation between singular vectors and issues to consider when trying to compute this correlation.

Chapter 3 contains many different Monte Carlo simulations performed to compute the average alignment in the multi-user singular vectors. The simulations begin with an independent and identically distributed (i.i.d.) complex Gaussian channel. These results are compared to those generated by the two ring channel model. In each of these simulations, different model parameters are varied in an effort to emulate different real world scenarios.

Chapter 4 provides simulated results of the impact of alignment in the singular vectors between users on multi-user sum capacity for the block-diagonalization algorithm. Two scalar correlation metrics are presented to give a single quantity representing correlation in the singular vectors to which the capacity can be compared.

Chapters 5 and 6 provide information on the MIMO wireless channel probing hardware, data collection experiments, and the results from the different experiments. Chapter 5 describes the measurement platform hardware design and construction as well as the signal processing involved in computing measured channel transfer matrices. Chapter 6 discusses the results of the different experiments performed and compares them with the two ring model in a methodical manner. Finally, Chapter 7 provides concluding remarks and suggestions for future research.

Chapter 2

MIMO Transmission Models, the SVD, and Singular Vector Alignment

This chapter explains the terminology and notation that will be used throughout the rest of this thesis. Section 2.1 briefly presents the extended SVA model (**S**aleh-**V**alenzuela model with **A**ngle-of-arrival and angle-of-departure (AOA/AOD) statistics) [5]-[7]. The SVA model can be easily extended to a two ring channel model that is described in Section 2.2. Section 2.3 gives a simple example that motivates the discussion of correlation in the singular vectors. In Section 2.4, a formal mathematical representation is given for describing alignment between singular vectors of the MIMO channels for two users. Finally, Section 2.5 shows how to extend results from using a single transmitter and two receivers to those results obtained from many transmitters and receivers through reciprocity and induction.

2.1 SVA Model Introduction

In this derivation and throughout the thesis, boldface uppercase and lowercase symbols denote matrices and vectors, respectively. Consider the point-to-point MIMO transmission scenario shown in Figure 2.1. Our received signal vector is given by

$$\mathbf{y} = \mathbf{H}\mathbf{x} + \mathbf{n}, \tag{2.1}$$

where the noise $\mathbf{n}$ is usually modeled as multivariate complex Gaussian

$$\mathbf{n} \sim \mathcal{CN}(\mathbf{0}, \sigma^2\mathbf{I}_N).$$

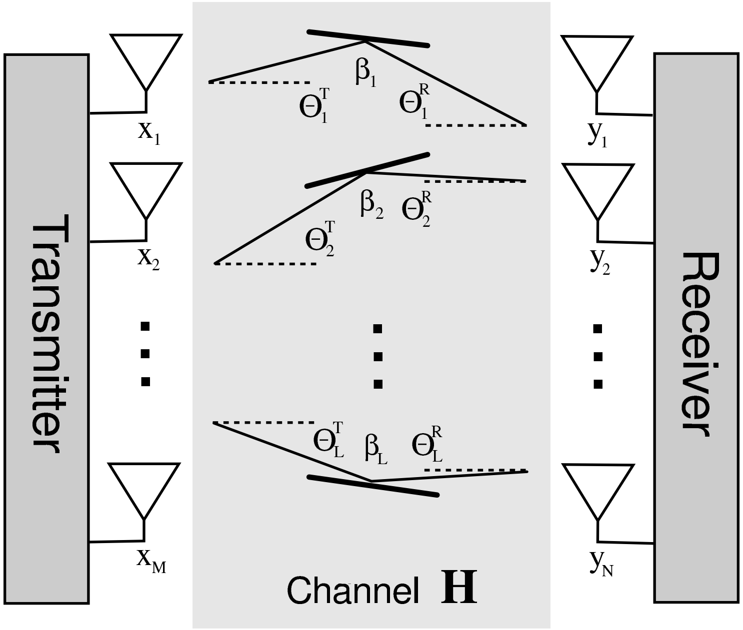

Figure 2.1: Ray-based model for the MIMO channel.

Table 2.1: Parameters for the SVA model channel response defined by (2.2)

Parameter	Description
l	Cluster number
k	Arrival number within a cluster
Θ_l^T	Mean angle of departure of rays in the lth cluster
Θ_l^R	Mean angle of arrival of rays in the lth cluster
ω_{kl}^T	Angle of departure of the kth transmit ray in the lth cluster, relative to Θ_l^T
ω_{kl}^R	Angle of departure of the kth receive ray in the lth cluster, relative to Θ_l^R
β_{kl}	Complex gain of the kth ray in the lth cluster
W_n^T	Steering vector for nth transmit antenna that includes the antenna gain pattern and transmitted phase variation
W_m^R	Steering vector for mth receive antenna that includes the antenna gain pattern and received phase variation

H_{mn} represents the complex gain from transmit antenna n to receive antenna m. Using the narrowband SVA model leads to the channel transfer function

$$H_{mn} = \sum_{l=0}^{L-1} \sum_{k=0}^{K-1} \beta_{kl} W_m^R(\Theta_l^R + \omega_{kl}^R) W_n^T(\Theta_l^T + \omega_{kl}^T). \tag{2.2}$$

Table 2.1 shows the meaning of the parameters in the narrowband SVA model. The steering vectors are defined as

$$W(\theta) = g(\theta) \exp\left[jk_0(x\cos\theta + y\sin\theta)\right],$$

where $g(\theta)$ is the gain pattern of the antenna of interest, k_0 is the free-space wavenumber, and (x, y) is the coordinate of the antenna.

Here, the model assumes that rays arrive in clusters in both space and time. For the narrowband case, we can assume that arrivals within a cluster of time are summed for each time period. These assumptions have been shown to fit well with empirical data [6], [7]. Note that this model is assuming plane wave propagation since the AOAs and AODs are the same for each element of the receive and transmit arrays respectively.

2.2 Two Ring Channel Model

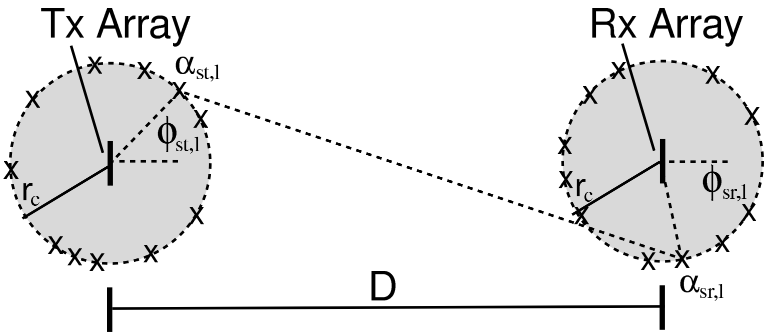

Figure 2.2: Two ring channel model

Figure 2.2 shows an example of the two ring channel model. Referring to the figure, the transmitter (Tx) and receiver (Rx) are each located at the center of a circle

Table 2.2: Parameters for the two ring model channel response defined by (2.3) and (2.4)

Parameter	Description
l	scatter number for both transmit ring and receive ring
$\alpha_{st,l}$	complex gain of lth scatterer on transmit ring
$\alpha_{sr,l}$	complex gain of lth scatterer on receive ring
$r_{tot,l}$	total distance traveled by ray l
$\mathbf{r}_{tn}$	vector location of transmit antenna n
$\mathbf{r}_{rm}$	vector location of receive antenna m
$\mathbf{r}_{st,l}$	vector location of lth scatterer on transmit ring
$\mathbf{r}_{sr,l}$	vector location of lth scatterer on receive ring

of scatterers of equal radius r_c. The centers of these two rings are a distance D apart and there are L scatterers per ring. The complex gain from transmit antenna m to receive antenna n can then be described as

$$H_{mn} = \sum_{l=1}^{L} \alpha_{st,l}\alpha_{sr,l}e^{-jkr_{tot,l}}, \tag{2.3}$$

Here,

$$r_{tot,l} = |\mathbf{r}_{tn} - \mathbf{r}_{st,l}| + |\mathbf{r}_{st,l} - \mathbf{r}_{sr,l}| + |\mathbf{r}_{sr,l} - \mathbf{r}_{rm}|, \tag{2.4}$$

so that the total distance is simply the sum of distances from transmit antenna through two scatterers to receive antenna. Table 2.2 gives the parameters for the two ring channel model as described in equations (2.3) and (2.4). Note that, for simplicity, cross terms between Tx scatterer l and Rx scatterer $k \neq l$ are not allowed so that the total channel response to receive antenna m from transmit antenna n can be described as a simple summation. Mathematically, this fits well with the SVA model. The first antenna in each array is placed at the center of its respective ring. Angle clustering and AOA/AOD in the SVA model can be created here by changing the distribution of the scatterers in the ring (by changing ϕ_l in Figure 2.2). The complex gains in the SVA model become the multiplication of $\alpha_{st,l}\alpha_{sr,l}$ in the two ring model.

The two ring channel model is an extension of the one ring model presented in [8]. The one ring model is considered useful because a base station is usually high above the average terrain. This allows for a base station to be modeled without any local scatterers. For more general indoor and outdoor wireless environments however, the two ring model is more suitable since it allows for more variation in AODs. To create a Monte Carlo simulation using this model, the scattering gains are generally distributed as zero-mean complex Gaussian random variables. We can fully describe the placement of each scatterer on its ring by the angle ϕ_l it creates with the line drawn between the center of the two rings. The angle for each scatterer can then be uniformly distributed for a rich multipath environment, or if a simulated transmission near a single wall is desired, then a Gaussian distribution of angles could be used whose mean corresponds to the midpoint of the wall between the two systems. Statistically, scatterer angle can also be used to model the orientation of the Tx and Rx arrays. For each realization of scatterer angles and gains, the full channel matrix is constructed element by element as described in equation (2.3).

The two ring model provides the benefit of an intuitive physical picture of the propagation channel. The physical placement of users within the model changes the resulting channel response, something that cannot be modeled by the SVA model. For example (actual results will be shown later), the local scatterers around two receivers can remain the same while one user moves relative to another, modeling how incoherent phase summation can change the channel response while the scattering environment is stationary. In the two ring model this simply requires changing the location parameters of one user. In the SVA model, this would be a complex simulation that is difficult to describe with the parameters given. Also, with the two ring model, the scatterers around the transmitting base station can remain the same, while all the mobile users can have independent scattering rings, thus emulating a broadcast or multiple access channel. Again, with the SVA model, it is impossible to keep a "local" scattering environment around a transmitter the same for all mobile users without adding complexity to the model. In chapter 3, many different cases will be simulated to try to emulate actual physical environments.

2.3 Simple Example for Use of the SVD

To motivate a full investigation into the correlation of singular vectors, a discussion of why the SVD is important to MIMO networks is warranted. This will be provided by a simple example of precoding and decoding parallel co-channel bitstreams. Here it is desired to use N transmit and receive antennas to communicate the vector

$$\mathbf{s}^{[k]} = \begin{bmatrix} s_1^{[k]} \\ s_2^{[k]} \\ \vdots \\ s_N^{[k]} \end{bmatrix}.$$

The SVD of $\mathbf{H}$ is

$$\mathbf{H} = \mathbf{U}\mathbf{S}\mathbf{V}^H.$$

We can precode the transmitted symbols as

$$\mathbf{x}^{[k]} = \mathbf{V}\mathbf{s}^{[k]},$$

leading to the receive signal vector

$$\begin{aligned} \mathbf{y}^{[k]} &= \mathbf{U}\mathbf{S}\mathbf{V}^H\mathbf{x}^{[k]} + \mathbf{n}^{[k]} \\ &= \mathbf{U}\mathbf{S}\mathbf{V}^H\mathbf{V}\mathbf{s}^{[k]} + \mathbf{n}^{[k]} \\ &= \mathbf{U}\mathbf{S}\mathbf{s}^{[k]} + \mathbf{n}^{[k]}. \end{aligned}$$

We finally decode the received vector (assuming $\mathbf{H}$ is known and full rank) using

$$\begin{aligned} \mathbf{z}^{[k]} &= \mathbf{U}^H\mathbf{y}^{[k]} \\ &= \mathbf{U}^H\mathbf{U}\mathbf{S}\mathbf{s}^{[k]} + \mathbf{U}^H\mathbf{n}^{[k]} \\ &= \mathbf{S}\mathbf{s}^{[k]} + \mathbf{n}'^{[k]}. \end{aligned}$$

The transformed noise vector distribution is

$$\mathbf{n}'^{[k]} \sim \mathcal{N}(\mathbf{0}, \sigma^2\mathbf{I}_N),$$

since $\mathbf{U}^H$ simply represents a rotation. Because $\mathbf{S}$ is diagonal, $\mathbf{z}^{[k]}$ contains the original desired symbol vector with each element independently scaled by the singular

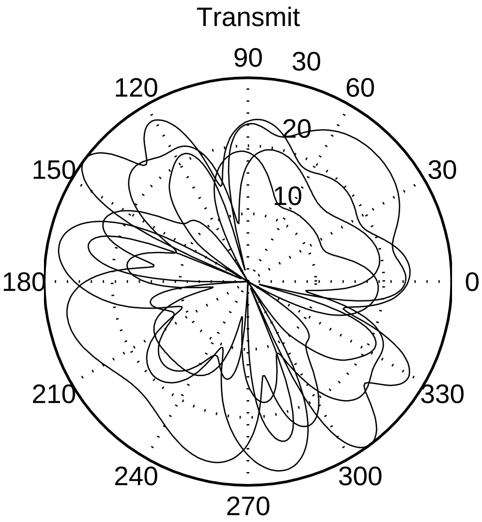

Figure 2.3: Example Tx eigenbeams

values and corrupted by additive noise. Therefore, the singular vectors of $\mathbf{H}$ can be considered a basis set for the space of interest.

The transformation $\mathbf{x}^{[k]} = \mathbf{V}\mathbf{s}^{[k]}$ describes a beamformer at the transmitter, referred to here as the *eigenbeamformer*. Each column of $\mathbf{V}$ represents the array weights for a specific data symbol in $\mathbf{s}^{[k]}$. Figure 2.3 shows the first four transmit eigenbeams for one example realization of an 8×8 complex Gaussian channel matrix $\mathbf{H}$. Similarly, each column in $\mathbf{U}^H$ represents the array weights for the receive eigenbeams.

2.4 Correlation in the Singular Vectors

Examining spatial correlation between individual elements of the channel matrix $\mathbf{H}$ may not give a complete representation of the channel behavior in multi-user MIMO environments. For example, while the correlation between antenna elements as a function of position becomes negligible for distances over a few wavelengths, this doesn't mean that the singular vectors are no longer aligned. In most of this thesis, we will cover a scenario with a single transmitting array (Tx) and two separate receiving arrays (Rx1 and Rx2). To examine the correlation in the singular vectors, the figures of merit desired are

$$\mathbf{R}_{\mathbf{VV}} = E\{\mathbf{V}_1^H \mathbf{V}_2\},$$

and

$$\mathbf{R}_{\mathbf{UU}} = E\{\mathbf{U}_1^H \mathbf{U}_2\},$$

where $\mathbf{V}_i$, and $\mathbf{U}_i$ are respectively the right and left singular matrices of receiver i. These operations produce a full matrix of correlations where the (m, n) element is the inner product of the m^{th} singular vector in Rx1 with the n^{th} singular vector in Rx2. This correlation can be interpreted as the alignment of the singular vectors in the N-dimensional complex space. For this reason, we will interchangeably use the terms correlation, inner product, and alignment throughout the thesis.

If we wanted a simple metric for how all singular vectors of equal position (same singular vector in the two receivers) are aligned, we could evaluate the quantities

$$\rho_{\mathbf{VV}} = \text{Tr}\{\mathbf{V}_1^H \mathbf{V}_2\}$$

and

$$\rho_{\mathbf{UU}} = \text{Tr}\{\mathbf{U}_1^H \mathbf{U}_2\},$$

where $\text{Tr}\{\mathbf{A}\}$ denotes the trace operation on matrix $\mathbf{A}$. These metrics provide a rough indication of the similarity of the dominant modes to each user. Another scalar metric that can be used that describes both equal and non-equal position alignment is

$$\rho = \frac{\mathbf{s}_1^H \mathbf{V}_1^H \mathbf{V}_2 \mathbf{s}_2}{\|\mathbf{s}_1\| \|\mathbf{s}_2\|}.$$

This metric will be more fully discussed in Section 4.3.

Problems arise when directly trying to compute the expectation for $\mathbf{R}_{\mathbf{VV}}$ and $\mathbf{R}_{\mathbf{UU}}$ with Monte Carlo simulations. This is due to the fact that the singular value decomposition is not unique. There is a symmetric phase ambiguity between each of the left and right singular vectors. To see this consider the following SVD,

$$\begin{aligned} \mathbf{H} &= \mathbf{U}\mathbf{S}\mathbf{V}^H \\ &= \mathbf{U}\boldsymbol{\Phi}\mathbf{S}\boldsymbol{\Phi}^H\mathbf{V}^H \\ &= \mathbf{U}'\mathbf{S}\mathbf{V}'^H, \end{aligned}$$

where

$$\mathbf{\Phi} = \begin{bmatrix} e^{j\phi_1} & 0 & \cdots & 0 \\ 0 & e^{j\phi_2} & \cdots & 0 \\ \vdots & \vdots & \ddots & \vdots \\ 0 & 0 & \cdots & e^{j\phi_n} \end{bmatrix}.$$

Each ϕ_k is an arbitrary phase. Note that this phase shift retains the properties of the singular value decomposition, i.e., $\mathbf{U}'$ and $\mathbf{V}'$ are still unitary matrices, and the result gives the same original matrix $\mathbf{H}$. Realizing this non-uniqueness of the SVD means that we cannot compute $\mathbf{R_{VV}}$ and $\mathbf{R_{UU}}$ directly since this phase ambiguity tends to reduce the apparent alignment if not appropriately handled. For example, when estimating $\mathbf{R_{VV}}$ and $\mathbf{R_{UU}}$ by Monte Carlo simulations with the sample mean, the ambiguity in the phase will cause the summation of each individual result to be meaningless. There are two methods to resolve this issue,

1. Compute $E\left\{\|\mathbf{V}_1^H\mathbf{V}_2\|\right\}$, and $E\left\{\arg\{\mathbf{V}_1^H\mathbf{V}_2\}\right\}$. Then combine these to form $\mathbf{R_{VV}}$, and do the same for $\mathbf{R_{UU}}$. Note that this is not the same as $\left\|E\{\mathbf{V}_1^H\mathbf{V}_2\}\right\|$.
2. Remove the phase ambiguity by scaling each singular vector such that its first element is purely real. Using this as $\mathbf{V}$ and $\mathbf{U}$ allows direct computation of $\mathbf{R_{VV}}$ and $\mathbf{R_{UU}}$.

There is a difference in the results when choosing method 1 or method 2. The second method will generally result in an $\mathbf{R_{VV}}$ or $\mathbf{R_{UU}}$ of smaller magnitude since the phase information is included in the expectation at each Monte Carlo realization. Unless otherwise noted, the second method is the one used throughout this thesis. This second method allows for some retention of information about the phase variation between any two singular vectors.

2.5 Reciprocity

Throughout this thesis, simulations and measurements will be performed using a single transmitting array and two receiving arrays. Reciprocity allows us to use these same results for the case of two transmitters and a single receiver. Suppose $\mathbf{H}_1$

represents the channel matrix from a single transmitter, Tx, to one of two receiving users, Rx1. $\mathbf{H}_2$ is then the channel matrix to the other receiver, Rx2. From these two channel matrices we compute $\mathbf{R}_{\mathbf{VV}}$, and $\mathbf{R}_{\mathbf{UU}}$. Now let $\mathbf{H}'_1$ represent the channel matrix from Rx1 to the transmitter Tx (reverse direction) and likewise for $\mathbf{H}'_2$. Then we have the following,

$$\begin{aligned} \mathbf{H}'_i &= \mathbf{H}_i^T \\ &= (\mathbf{U}_i \mathbf{S}_i \mathbf{V}_i^H)^T \\ &= \mathbf{V}_i^* \mathbf{S}_i^T \mathbf{U}_i^T . \end{aligned}$$

This then results in

$$\mathbf{R}'_{\mathbf{VV}} = \mathbf{U}_1^T \mathbf{U}_2^* = \mathbf{R}^*_{\mathbf{UU}}$$

and

$$\mathbf{R}_{\mathbf{UU}}{}' = \mathbf{V}_1^T \mathbf{V}_2^* = \mathbf{R}^*_{\mathbf{VV}}.$$

Extensions to many transmitters and receivers can then be drawn easily by induction.

2.6 Chapter Summary

This chapter outlined briefly the narrowband SVA model for representing physical MIMO channels. The two ring model was then presented and it was argued that such a model can retain the capabilities of the SVA model while providing a better physical match to the channel physical properties. The discussion also demonstrated how this two ring model allows for easier modeling of multi-user scenarios, especially movement of one user with respect to another.

The relevance of correlation in the singular vectors was introduced with a simple MIMO channel coding example that exploits the SVD of the channel matrix $\mathbf{H}$. A mathematical description of the figures of merit for alignment between singular vectors of two users was given. The chapter closed with a discussion on implementation issues for computing these figures of merit and a demonstration of how to make extensions to many transmitting and receiving arrays.

Chapter 3

Singular Vector Correlation Simulations

As described previously, the right singular vectors $[\mathbf{v}_1\ \mathbf{v}_2\ \cdots\ \mathbf{v}_{N_T}]$ form a unitary basis for the right range space of $\mathbf{H}$. In the single user case, capacity can be achieved when $\mathbf{H}$ is known by precoding the transmitted vector data stream with these right singular vectors [12]. The water-filling solution is then applied to determine the weights for each singular vector eigenbeam. For the multi-user case, other algorithms are described which also take advantage of the SVD of $\mathbf{H}$ (see, for example [11]). This suggests that some investigation should be performed into the similarity of the singular vectors of the transfer matrices for different users. Here we will examine the case of a single transmitter array and two receiver arrays. Generalizations can then be drawn to the case of multiple transmitters (through reciprocity) or more than two receivers (by induction). We begin in this chapter with some modeling work.

Section 3.1 gives the statistical results for an independent and identically distributed (i.i.d.) complex normal channel matrix to each user. The bulk of the chapter, Section 3.2, describes the results of various Monte Carlo simulations using the two ring channel model. The model is tailored to different possible real world circumstances to allow investigation of the results for different scenarios.

3.1 Gaussian i.i.d. Channel Matrix

Much of the information theoretical work on MIMO wireless systems relies on a channel model with the multivariate i.i.d. complex normal distribution. Although this simple channel model ignores important system and channel characteristics, it can provide a reference point for correlation in the singular vectors. This observation motivates a study of $\mathbf{R_{VV}}$ and $\mathbf{R_{UU}}$ when the channel matrix can be described as

$$\text{vec}(\mathbf{H}) \sim \mathcal{CN}(\mathbf{0}, \mathbf{I}).$$

It is difficult to derive a closed form result for the expectation required in computing $\mathbf{R_{VV}}$ and $\mathbf{R_{UU}}$ since the singular value decomposition is involved. One way to view the problem is to assume that each element of $\mathbf{R_{VV}}$ and $\mathbf{R_{UU}}$ is the same as the value attained when looking at the expectation of the inner product of two random vectors in complex N space that are constrained to be unit length. In other words, since $\mathbf{H}$ is i.i.d. complex normal, it will generally be full rank. This means that for a square $\mathbf{H}$, $\mathbf{V}$ and $\mathbf{U}$ will also be full rank and will form an orthonormal set of basis vectors for $\mathcal{R}\{\mathbf{H}\} = \mathcal{R}\{\mathbf{H}^T\}$. Here, $\mathcal{R}\{\mathbf{A}\}$ denotes the range of $\mathbf{A}$. For each realization of $\mathbf{H}$, $\mathbf{V}$ and $\mathbf{U}$ will be random rotation matrices, but their columns will all be of unit length.

A large amount (100,000) of Monte Carlo realizations was performed to find $\mathbf{R_{VV}}$ and $\mathbf{R_{UU}}$ for the case of $\text{vec}(\mathbf{H}) \sim \mathcal{CN}(\mathbf{0}, \mathbf{I})$. In this simulation, each element of $\mathbf{R_{VV}}$ and $\mathbf{R_{UU}}$ were of equal value, and a single number describes the result for each element of both correlation matrices. The phase of each metric was negligible. These simulation results were identical to simulations performed computing the average inner product of length N i.i.d. complex normal random vectors which were scaled so that their first element was purely real and had unit norm, which verifies the statements in the preceding paragraph. Table 3.1 contains the values found for $\mathbf{R_{VV}}$ and $\mathbf{R_{UU}}$ for these simulations.

3.2 Two Ring MIMO Channel Model Monte Carlo Simulations

This section describes various Monte Carlo simulations based upon the two ring channel model discussed in chapter 2. Different aspects of the two ring model are changed in order to simulate real world scenarios. These scenarios include rich indoor multipath environments, semi-rich outdoor environments, and situations with few dominant paths.

Table 3.1: i.i.d. Gaussian simulation results

$N_R \times N_T$	$\mathbf{R_{VV}}_{m,n}$, $\mathbf{R_{UU}}_{m,n}$
2×2	0.4447
4×4	0.2088
8×8	0.1013
10×10	0.0805
16×16	0.0499

3.2.1 Same Ring for Both Receivers

The first two ring scenario simulated was with both receivers (Rx1 and Rx2) located within the same ring of scatterers. For this case, Rx1 remained at the center of the receiver scatterer ring while Rx2 was moved from 0-1000 wavelengths (λ) linearly away from Rx1 in the direction away from the transmitter. The parameters of the model used in the simulation are given in Table 3.2. The antenna separation in each receiver and transmitter array was $\lambda/2$. This simulation was repeated for 1000 Monte Carlo realizations, and the expected value of correlation between singular vectors in the two receivers was approximated using the sample mean.

Figure 3.1 shows the resulting correlation between the right singular vectors of Rx1 and Rx2 versus separation in wavelengths, while Figure 3.2 shows the correlation between the left singular vectors versus separation in wavelengths for a 4×4

Table 3.2: Two ring simulation parameter values.

Parameter description	Parameter value
Receiver separation	$d = 0{-}1000\lambda$
Array element separation	$\lambda/2$
Number of scatterers	$L = 20$
Ring separation	$D = 10000\lambda$
Ring radius	$r_c = 1000\lambda$
Scatterer angle distribution	$\theta_{st,l}, \theta_{sr,l} \sim \mathcal{U}(0, 2\pi)$
Scatterer complex gain distribution	$\alpha_{st}, \alpha_{sr} \sim \mathcal{CN}(\mathbf{0}, \mathbf{I})$

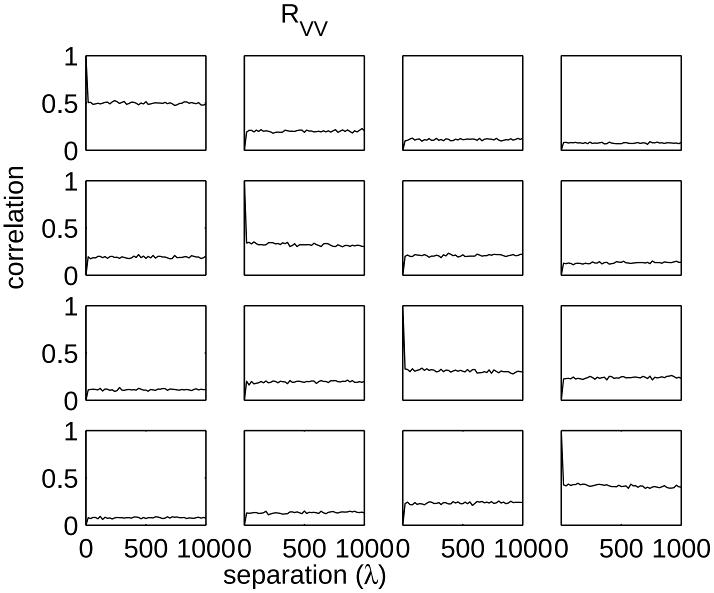

Figure 3.1: Alignment between right singular vectors. Same ring for both receivers, 4×4 MIMO.

MIMO network. The correlation in the right singular vectors for the 4×4 case is nearly independent of distance, and for the left singular vectors it is a weak function of distance. The interesting thing to note here is that the equal position singular vectors are more aligned than for the i.i.d. Gaussian case. Figures 3.3 and 3.4 show that the case is similar for a 8×8 MIMO network. These 8×8 results better show another interesting fact about the correlation in the singular vectors: the further apart in position two singular vectors are, the less likely they are to be aligned. Furthermore, these correlation figures in $\mathbf{R_{UU}}$ approach that of the i.i.d. Gaussian case as the distance d gets large. As Rx2 moves away from Rx1, their eigenbeams became increasingly uncorrelated since the Rx scatterers differed more and more in angle and distance with respect to each receiving array. For this simulation, this is when Rx2 approaches the envelope of the Rx ring.

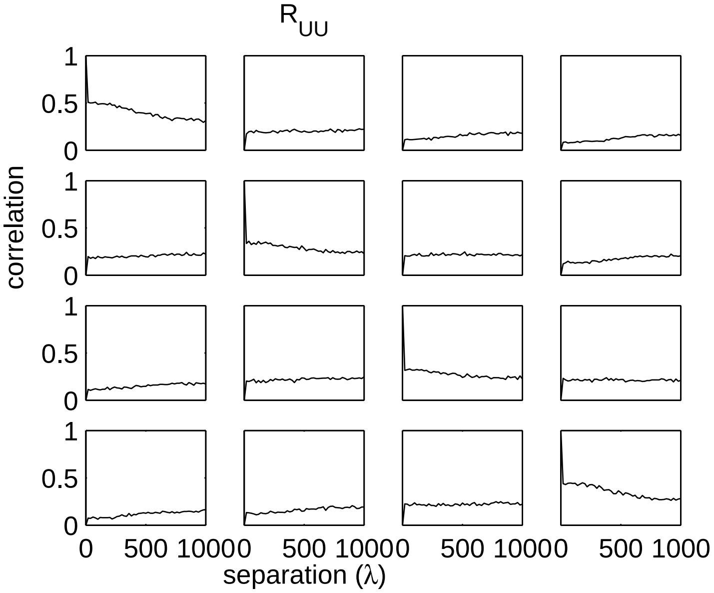

Figure 3.2: Alignment between left singular vectors. Same ring for both receivers, 4×4 MIMO.

In these plots, only the magnitude of $\mathbf{R_{VV}}$ and $\mathbf{R_{UU}}$ are shown. The phase was negligible (close to zero) for all expected singular products that were greater than zero. If the expected inner product $E[\mathbf{v}_{1_i}^H \mathbf{v}_{2_j}]$ was zero then the phase was random (and unimportant anyway). This is the same for all simulations in this chapter as well as for the measured results in Chapter 6.

Understanding that the right singular vectors comprise the eigenbeams for the transmitter, one might expect much more correlation in $\mathbf{R_{VV}}$ since both the transmitter and receiver rings are identical for both receiving users. This might suggest that the transmitter should direct its transmitted power towards the same scatterers within the Tx ring in order to optimize throughput to both users. However, as the second receiver travels within the Rx ring away from Rx1, the fast fading characteristics of the model cause the phases of each scatterer ray to add incoherently. This phase interference results in different eigenbeams ($\mathbf{V}$) at the transmitter. In other words, different Tx scatterers become emphasized as their respective Rx scatterers add constructively and destructively in phase at each receiver. Recall that for this

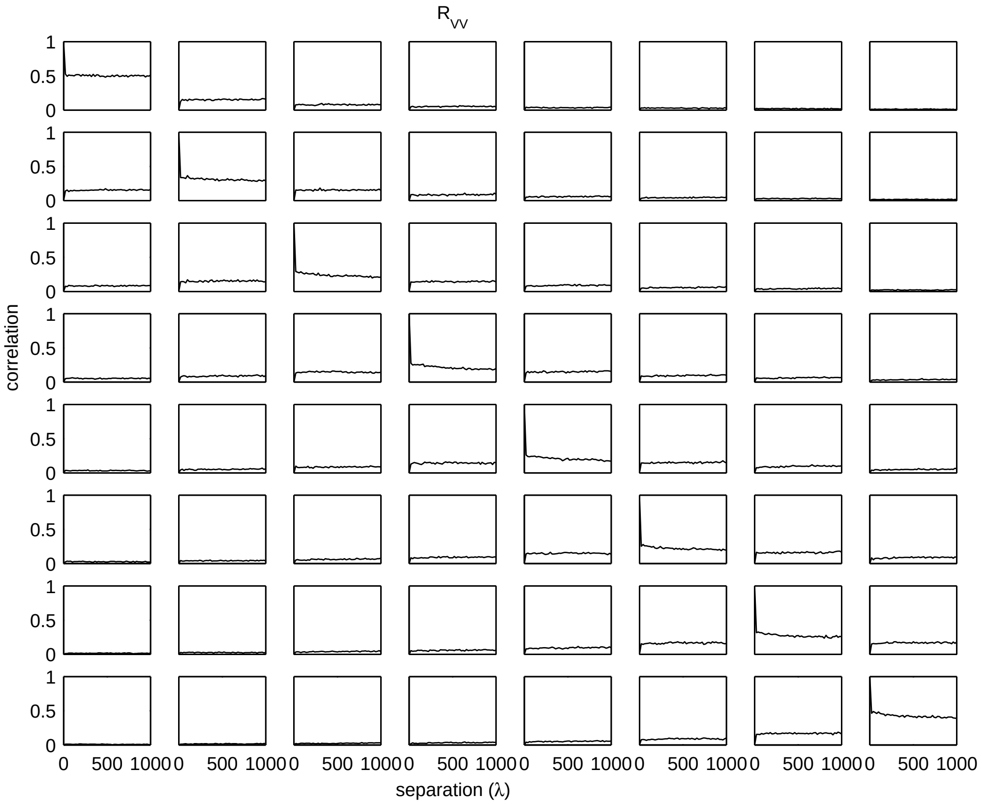

Figure 3.3: Alignment between right singular vectors. Same ring for both receivers, 8×8 MIMO.

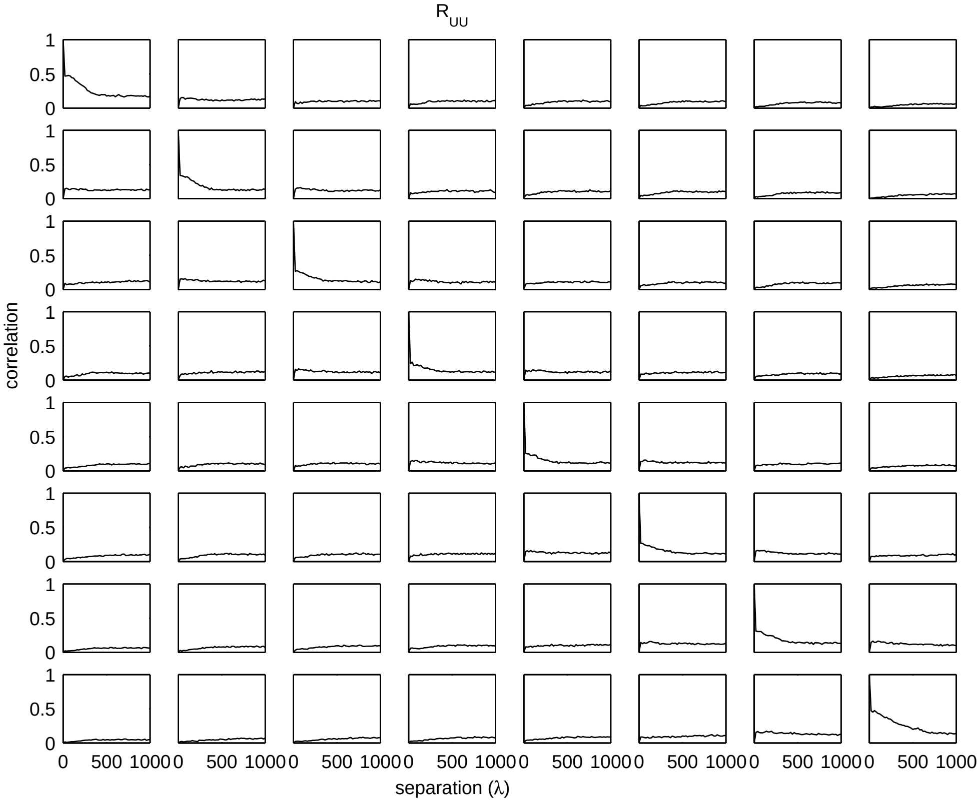

Figure 3.4: Alignment between left singular vectors. Same ring for both receivers, 8×8 MIMO.

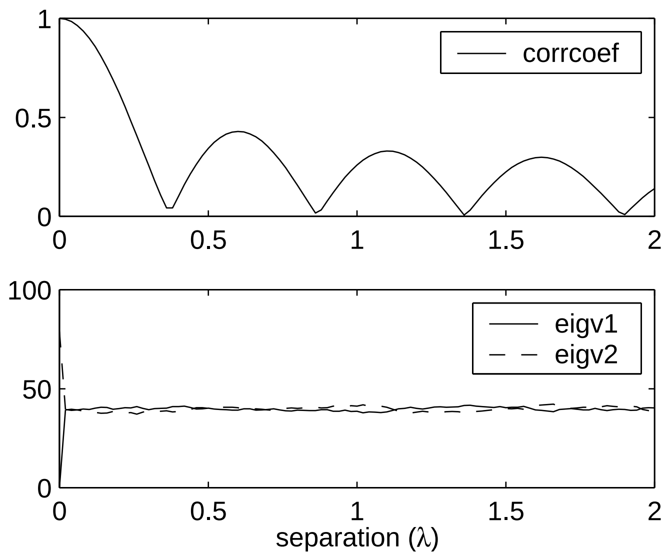

Figure 3.5: Correlation coefficient between H_{11} and H_{12} and eigenvalues of $\mathbf{HH}^H$ from 0-2λ. Same ring for both receivers, 2×2 MIMO.

two ring model, there are no cross-terms between Tx and Rx scatterers, i.e., each Tx scatterer is paired with only one Rx scatterer. Looking at the graphs of Figures 3.1 and 3.3 we see that this effect is independent of separation distance, which agrees with the argument given above.

An element of this simulation that should be emphasized is the difference between array element spatial correlation and singular vector alignment as a function of user separation distance. Figures 3.5 and 3.6 help to illustrate this difference. Here, a 2×2 MIMO scenario is employed, and the correlation coefficient for H_{11} and H_{12} is plotted for 0 - 2λ and 0 - 500λ. This correlation coefficient is

$$\rho(H_{11}, H_{12}) = \frac{E\{H_{11}H_{12}^*\}}{\sqrt{E\{H_{11}H_{11}^*\}E\{H_{12}H_{12}^*\}}},$$

where we have assumed zero mean channel coefficients. The spatial correlation between the two antennas becomes negligible at separation distances over 2λ while Figures 3.1 - 3.4 demonstrate that the alignment in the singular vectors persists.

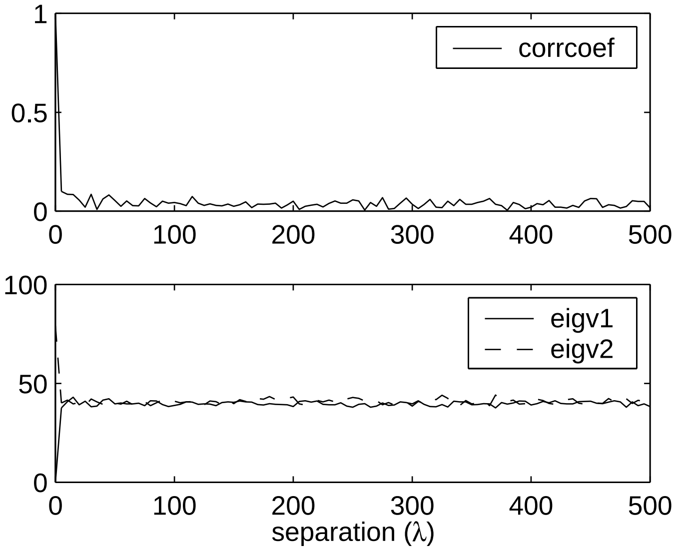

Figure 3.6: Correlation coefficient between H_{11} and H_{12} and eigenvalues of $\mathbf{HH}^H$ from 0-500λ. Same ring for both receivers, 2×2 MIMO.

Also shown in these figures are how the two eigenvalues of $\mathbf{HH}^H$ change over separation distance. From this we see that the expected singular values are fairly constant over time, even though the correlation in the left singular vectors slowly decays. The fact that these eigenvalues are nearly equal tells us that this simulated case provides us with a rich multipath channel environment. Only when the two antennas are co-located do we see that the channel matrix $\mathbf{H}$ becomes singular.

3.2.2 Different Rings for Two Receivers

A multipath rich indoor environment will have a large number of scatterers that are fairly close to the receivers. This may mean that as one receiver moves away from the other, they will have different scatterers around them that they interact with. This provides the motivation for this simulation scenario where we will realize a separate Rx ring for each receiver, Rx1 and Rx2. The same parameters are used here as in Section 3.2.1 (see Table 3.2).

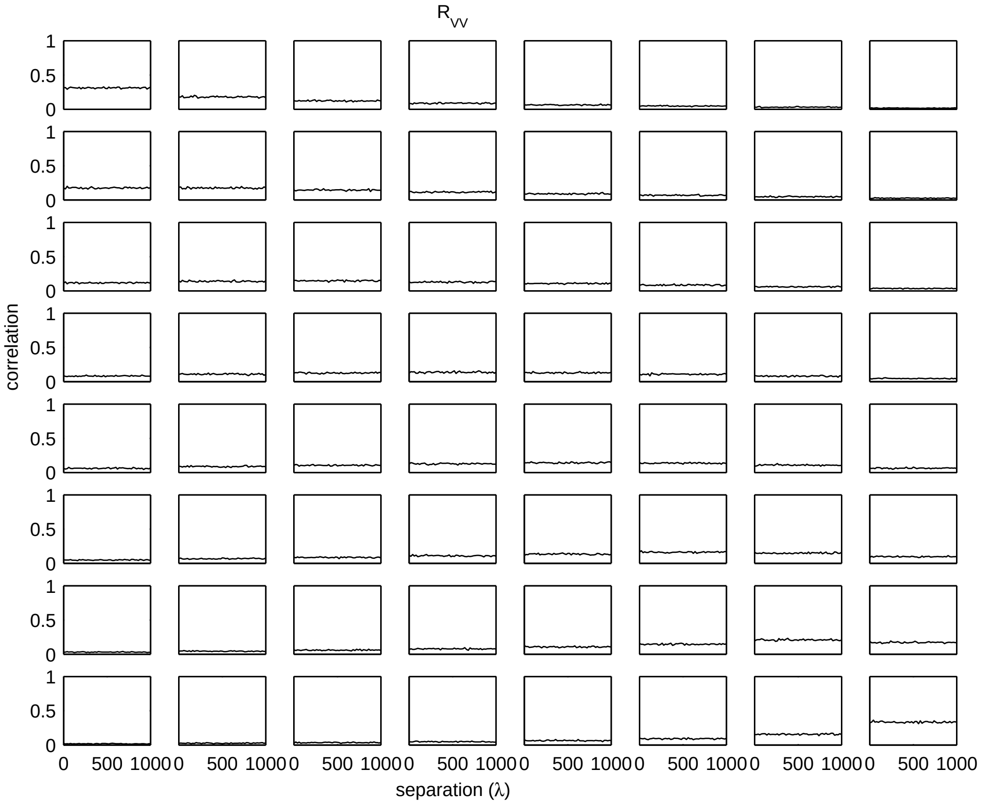

Figure 3.7: Alignment between right singular vectors. Different ring for each receiver, 8×8 MIMO.

The results of this simulation were similar for 2×2, 4×4, 8×8, and 10×10. Only the 8×8 case is shown and is exemplary of the other cases. Figures 3.7 and 3.8 show that for this case, correlation is not a function of separation distance between receivers. This, of course, is expected since they always see different scatterers. What is interesting here, however, is that the correlation in equal position right singular vectors is slightly greater than that of the left singular vectors. This arises from the fact that Rx1 and Rx2 are still interacting with the same scatterers associated with the transmitter. Although the Rx scatterer complex gains are independent between the two users, the Tx scatterer gains are equal. If a single complex gain associated with each ray path was used as in the SVA model, then this characteristic would not be observed. Separate complex gains associated with a transmit scatterer and

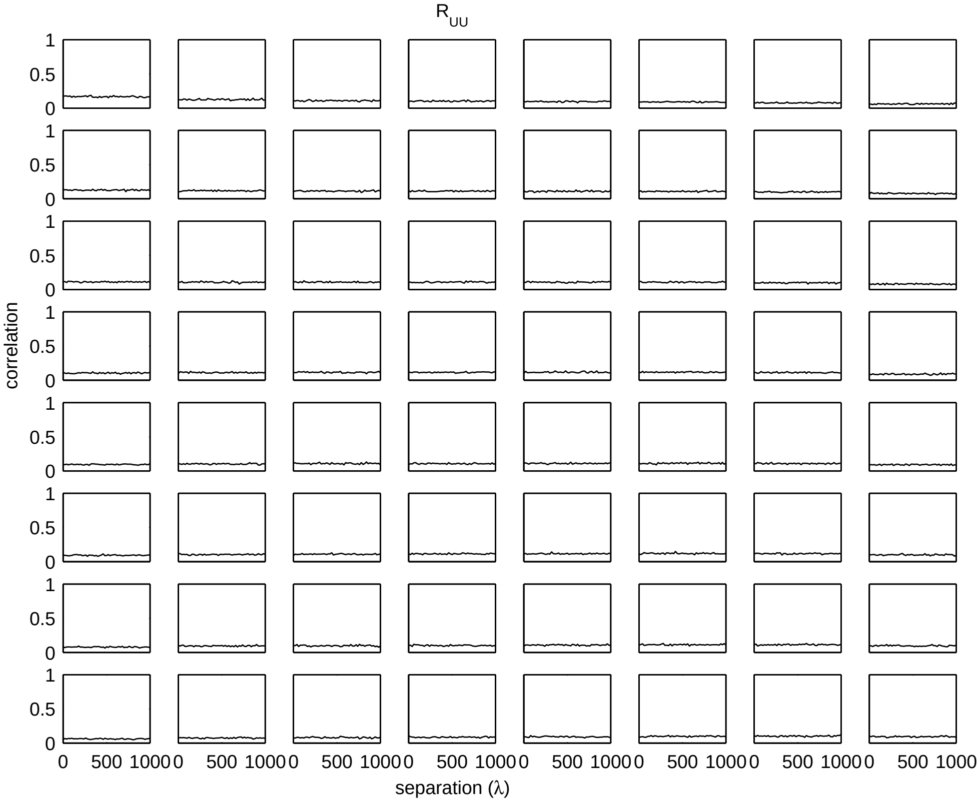

Figure 3.8: Alignment between left singular vectors. Different ring for each receiver, 8×8 MIMO.

its respective receiver scatterer is more intuitive to a real world model. Of course, this is still a simplification since in a real world transmission, each received ray can result from various complex physical phenomena such as diffusion, diffraction, many reflections, etc.

Comparing these results more closely with those of Section 3.2.1, we see that $\mathbf{R_{UU}}$ for independent Rx rings is equal to the same value that $\mathbf{R_{UU}}$ converged to in Figure 3.4. This is also roughly the same value as given by the i.i.d. Gaussian case. This reasons well since in this simulation receiver rings were independent, leading to unrelated eigenbeams between the two receivers.

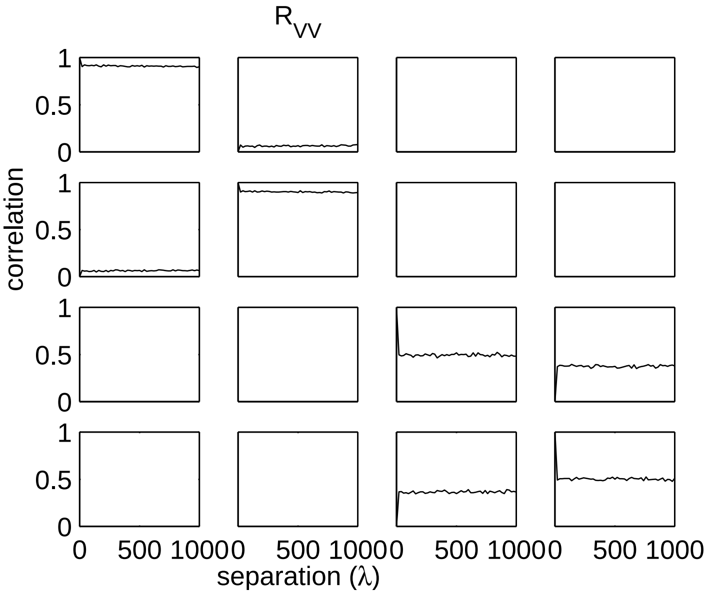

Figure 3.9: Alignment between right singular vectors. Two scatterers per ring, 4×4 MIMO.

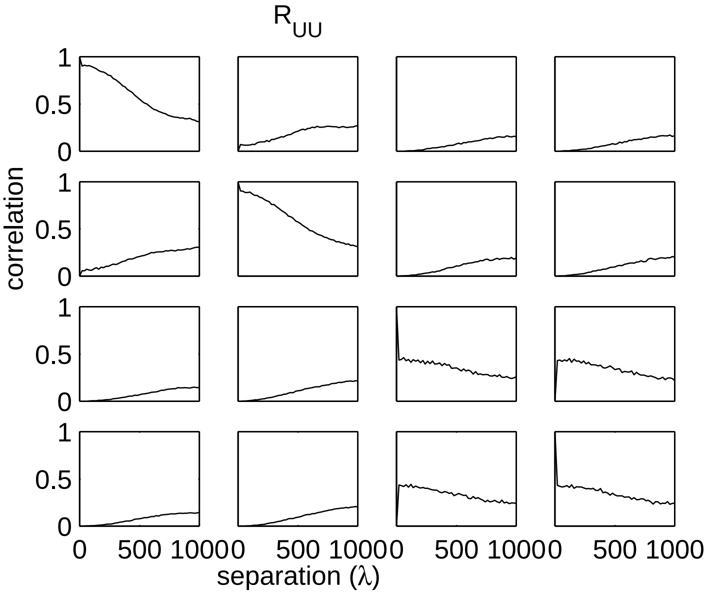

Figure 3.10: Alignment between left singular vectors. Two scatterers per ring, 4×4 MIMO.

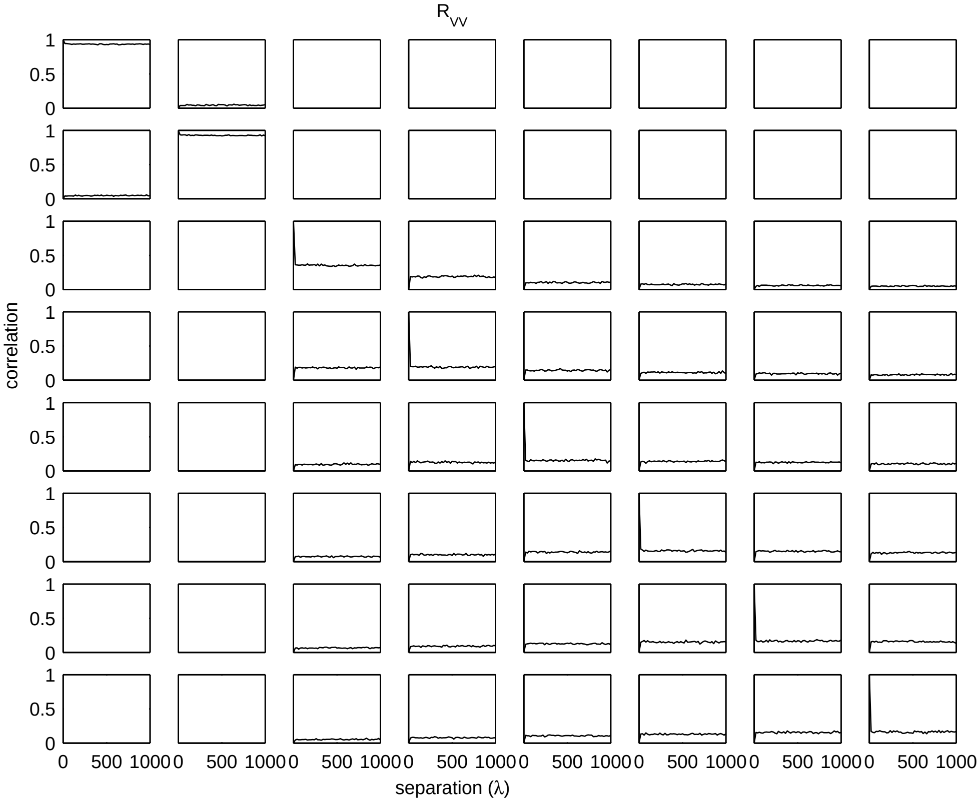

Figure 3.11: Alignment between right singular vectors. Two scatterers per ring, 8×8 MIMO.

3.2.3 Small Number of Scatterers

We now consider the case where the propagation channel is characterized by a line of sight path and a single reflection. For this case, the channel matrix will be rank deficient for array sizes larger than two elements. For this simulation, the parameters are the same as in Table 3.2, except that the number of scatterers is $L = 2$. The same scattering ring is used for both receivers to see the effect of user separation distance. As before, the results of this simulation for large separations converge to those obtained for independent scatterer rings for the two receivers.

Figures 3.9 and 3.10 show the results of this simulation for the 4×4 MIMO case and Figures 3.11 and 3.12 show the results for the 8×8 MIMO case. In all of these figures, we see that since there are only two scatterers per ring, **H** is rank

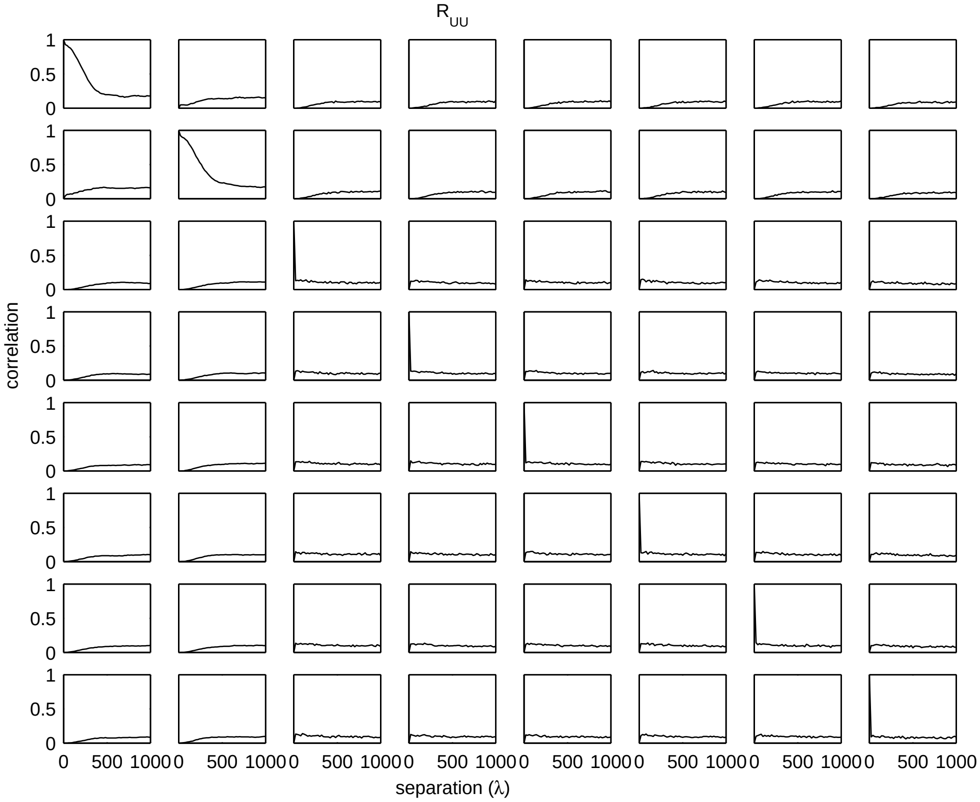

Figure 3.12: Alignment between left singular vectors. Two scatterers per ring, 8×8 MIMO.

deficient. Thus, the first two singular vectors correspond to the transmission modes that have the largest singular values. We see clearly from the 8×8 figures that this leads to closely aligned right singular vectors independent of distance. In the left singular vectors, the first two singular vectors become less correlated over distance until they converge to what an i.i.d. Gaussian distributed channel matrix would give. Note that since the rest of the singular vectors lie in the null space of $\mathbf{H}$ which is of effective rank 6, they can be randomly aligned as long as they span this null space. Since there are only two right singular vectors in the 4×4 case that must span a null space of effective rank 2, we see that these have nearly .44 correlation, similar to that of the 2×2 i.i.d. Gaussian case. The difference here of course is in the length of the singular vectors. Again, for the 4×4 case, the right singular vectors are independent of distance due to the reasons discussed in Section 3.2.1, and the left singular vectors approach the i.i.d. Gaussian case. One final thing to note is that the first two rows and columns of each figure in this section show that, as should be expected, the right singular vectors that lie within the range of $\mathbf{H}^H$ have no correlation with those in the null space of $\mathbf{H}$. This is also true of the left singular vectors up until the separation distance is enough to cancel this effect.

3.2.4 Nonuniform Distribution in Angle of Scatterers

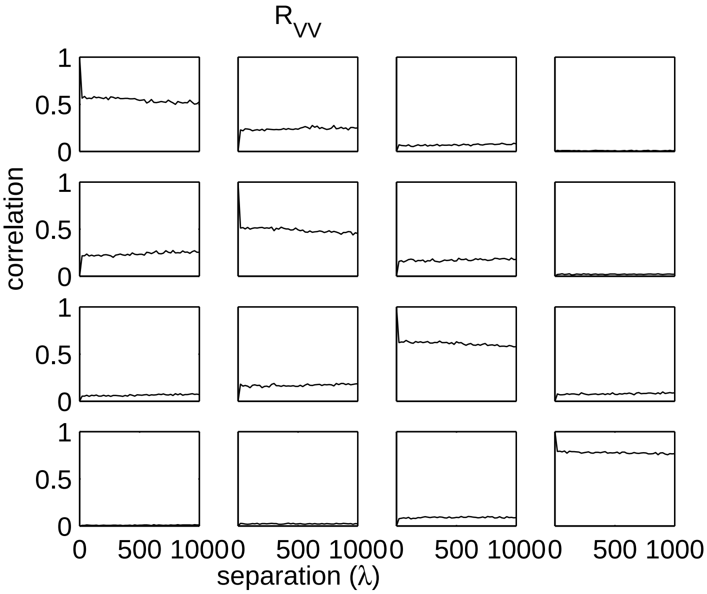

Figure 3.13: Alignment between right singular vectors. Nonuniform distribution in angle, 4×4 MIMO.

Scatterer angle of arrivals have been modeled successfully as a Laplacian random variable [4], [6] within each cluster of the SVA model. The clusters have been shown in the same references to be distributed uniformly. Throughout this discussion using the two ring model, each scattering angle has been representative of the mean angle of rays within a cluster in the SVA model. In effect, we have been ignoring

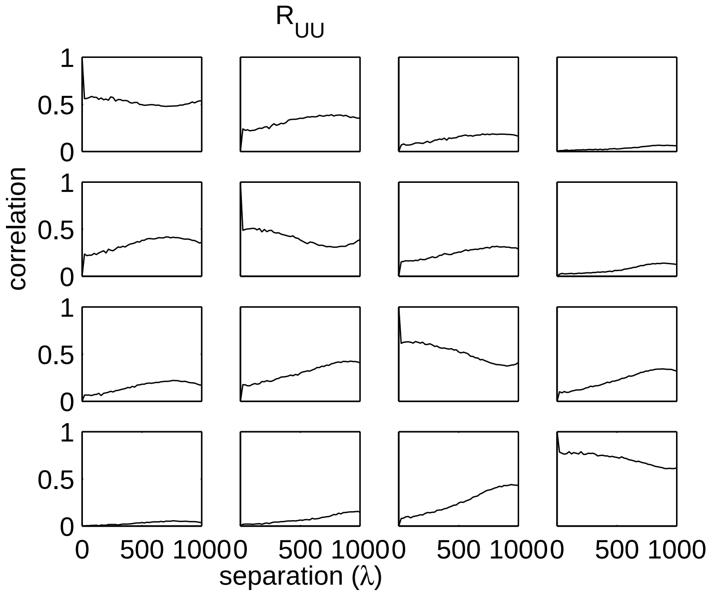

Figure 3.14: Alignment between left singular vectors. Nonuniform distribution in angle, 4×4 MIMO.

the effects of this random distribution in angle for each cluster. This assumption is reasonable if the variance of the aforementioned Laplacian distribution is small compared to the available resolution of the antenna array. This resolution is determined by the number of antenna elements in the array and the directivity of each antenna element.

For transmission near a single rough wall, we can assume a diffuse scattering environment where most of the scatterers are located along the wall near the midpoint between the transmitter and receiver. This case may be modeled with the two ring model by assuming a nonuniform distribution of scattering angles in each ring. For this simulation, a Gaussian distribution is used for scattering angles with non-zero mean and $\pi/10$ variance. We can, of course, assume a more complex model similar to that of the general SVA model, but here the desire is to examine the effects of non-uniform scattering angle distribution. The two ring model parameters for this simulation are the same as in Table 3.2, except of course for the distribution of $\theta_{st,l}$ and $\theta_{sr,l}$. The same scattering ring is again used for both receivers. The scatterers

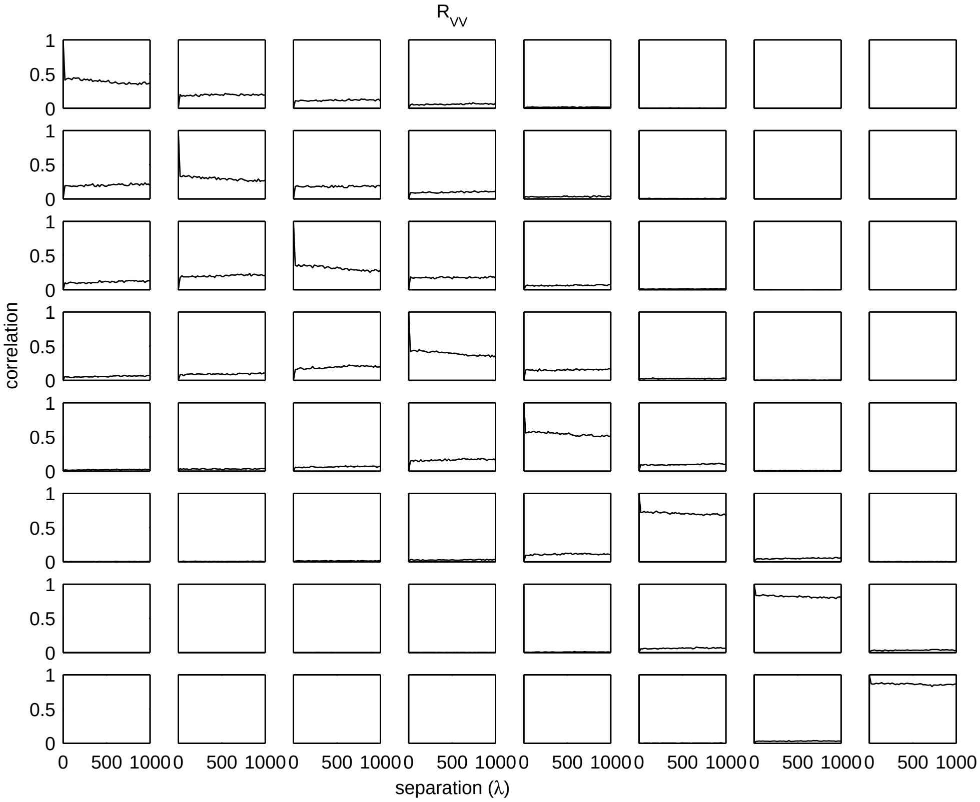

Figure 3.15: Alignment between right singular vectors. Nonuniform distribution in angle, 8×8 MIMO.

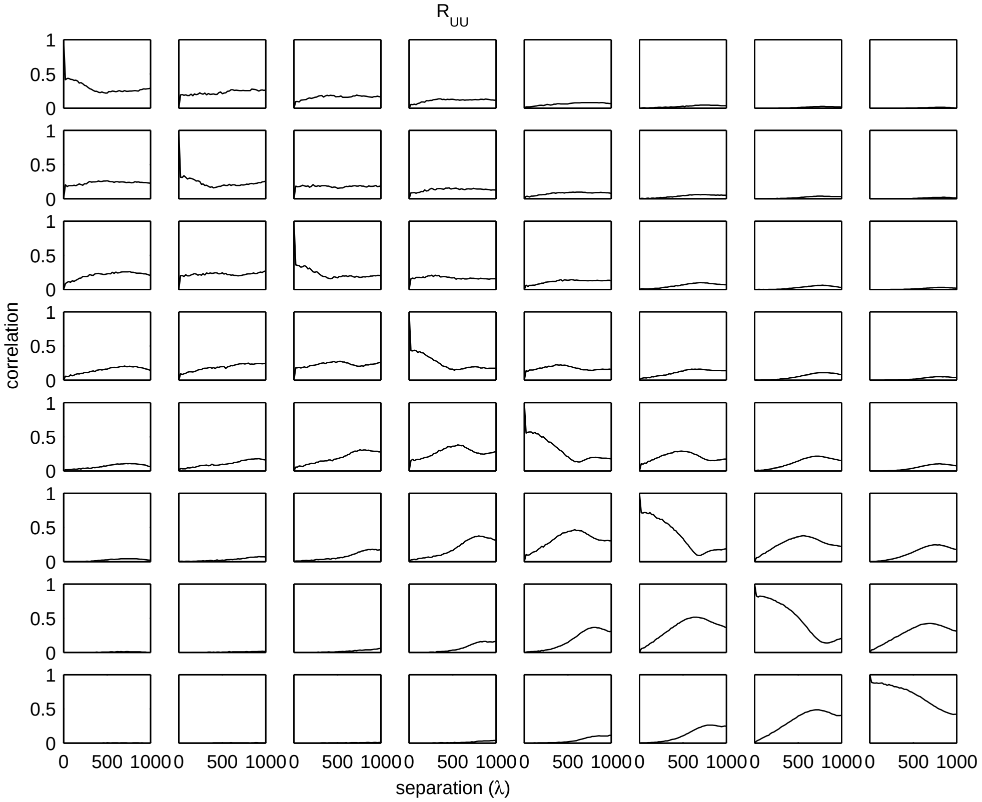

Figure 3.16: Alignment between left singular vectors. Nonuniform distribution in angle, 8×8 MIMO.

are distributed with

$$\mu_{Tx} = \frac{\pi}{4},\ \mu_{Rx} = \frac{-\pi}{4},\ \text{and}\ \sigma_{Tx}^2 = \sigma_{Rx}^2 = \frac{\pi}{10}.$$

Figures 3.13 and 3.14 show the results for the 4×4 MIMO case and Figures 3.15 and 3.16 show the results for the 8×8 MIMO case. Here we see a slow decrease in the correlation of the left singular vectors with increased separation, while the correlation in the right singular vectors remains nearly constant, following the same trends as previously observed. The increase in correlation in the right singular vectors around 800λ is an artifact of the model, and shouldn't be considered to accurately model a real world situation. This occurs when Rx2 passes the mean position of scatterers on the receive ring. In fact, if we instead choose $\mu_{Rx} = \frac{\pi}{3}$ then at $d = r_c = 1000\lambda$ high correlation between the two receivers would be seen, with nearly full correlation for smaller variance in the angle. While it is possible that a situation could occur such that the receivers could see the same scatterers in this manner, it is highly unlikely.

3.3 Chapter Summary

This chapter presented several Monte Carlo simulation results for both the i.i.d. complex normal channel matrix $\mathbf{H}$ and various two ring model setups. The i.i.d. complex normal channel serves as a description of a statistically uncorrelated channel. In this case it was shown that this correlation in $\mathbf{R_{VV}}$ and $\mathbf{R_{UU}}$ is the expectation of the inner product for any two random vectors in complex N space.

The two ring simulations conducted attempted to simulate various real world applications by intuitively changing parameters of the model. Through all these simulations the versatility of the two ring model is exemplified. In all scenarios, $\mathbf{R_{VV}}$ generally showed more correlation than $\mathbf{R_{UU}}$ since the transmission model to each receiving user employed the same scattering ring around the transmitter. It was shown that if the receivers are within the same scattering ring (but in different locations within the ring), $\mathbf{R_{UU}}$ shows much more correlation than for the case where different rings are employed around each receiver. In this latter case, $\mathbf{R_{UU}}$ shows correlation only slightly higher than that of the i.i.d. complex normal channel.

Chapter 4

Capacity Simulations

Knowing how closely the singular vectors correlate with each other can provide good analytical insight into the MIMO wireless channel. In short, if singular vectors of equal position in the two receivers are closely aligned, then the transmitter is using nearly the same modes of propagation to each receiver. The logical question then becomes how this correlation effects sum capacity. One representative algorithm will be used to aid in understanding this effect and is presented briefly in the first section of this chapter. This algorithm applies to the downlink broadcast channel and presents a sub-optimal solution that leads to relatively simple transmitter and receiver signal processing. Its maximum information rate does approach the theoretical sum capacity at high SNR. Two scalar metrics are used to examine the effects of alignment in the singular vectors on achievable rates. The chapter closes with a brief discussion on capacity where the total number of receive antennas exceeds the total number of transmit antennas.

4.1 The Block-Diagonalization Algorithm, $N_R \leq N_T$

In [11], a constrained solution is given for a multi-user downlink channel where the total number of receive antennas N_R is less than or equal to the total number of transmit antennas N_T. The algorithm that implements this solution is known as "block-diagonalization." In order to summarize the block-diagonalization algorithm, we must first introduce some notation. Here we assume a model much like that described in (2.1), where we have one base station and K users with the signal received at the j^{th} receiving user being expressed as

$$\begin{aligned}\mathbf{y}_j &= \sum_{i=1}^{K} \mathbf{H}_j \mathbf{M}_i \mathbf{s}_i + \mathbf{n}_j \\ &= \mathbf{H}_j \mathbf{M}_j \mathbf{s}_j + \mathbf{H}_j \tilde{\mathbf{M}}_j \tilde{\mathbf{s}}_j + \mathbf{n}_j.\end{aligned}$$

$\mathbf{M}_j$ is the modulation matrix (precoding) for user j and $\tilde{\mathbf{M}}_j$ is the modulation matrix for all users other than j expressed as

$$\tilde{\mathbf{M}}_j = [\mathbf{M}_1 \ \cdots \ \mathbf{M}_{j-1} \ \ \mathbf{M}_{j+1} \ \cdots \ \mathbf{M}_K].$$

We will also define $\tilde{\mathbf{H}}_j$ similarly to $\tilde{\mathbf{M}}_j$, or

$$\tilde{\mathbf{H}}_j = \left[\mathbf{H}_1^T \ \cdots \ \mathbf{H}_{j-1}^T \ \ \mathbf{H}_{j+1}^T \ \cdots \ \mathbf{H}_K^T\right]^T.$$

Since $N_T \geq N_R$, we can force $\mathbf{M}_j$ to lie in the null space of $\tilde{\mathbf{H}}_j$, thus forcing the interference from the transmission destined to other users to zero. To see this, we take the SVD of $\tilde{\mathbf{H}}_j$ as

$$\tilde{\mathbf{H}}_j = \tilde{\mathbf{U}}_j \tilde{\mathbf{S}}_j \left[\tilde{\mathbf{V}}_j^{(1)} \ \ \tilde{\mathbf{V}}_j^{(0)}\right]^H.$$

$\tilde{\mathbf{V}}_j^{(0)}$ forms a basis for the null space of $\tilde{\mathbf{H}}_j$, and its columns are then candidates for the modulation matrix $\mathbf{M}_j$. If we only require a subspace of the span of $\tilde{\mathbf{V}}_j^{(0)}$, then we can choose this subspace by setting

$$\mathbf{V}_j = \tilde{\mathbf{V}}_j^{(0)} \mathbf{V}_j^{(1)},$$

where $\mathbf{V}_j^{(1)}$ are the first right singular vectors of $\mathbf{H}_j \tilde{\mathbf{V}}_j^{(0)}$. This maximizes information rate to user j under the constraint of zero co-channel interference.

To summarize, since this algorithm makes use of the fact that for $N_T \geq N_R$, we are guaranteed that the null space of $\tilde{\mathbf{H}}_j$ is large enough to support R_j data streams to user j, where R_j is the rank of $\mathbf{H}_j$. This fact becomes important when analyzing the effect of singular vector correlation on the capacity of the block-diagonalization method. The block-diagonalization algorithm can be summarized as follows:

Sum Capacity Block Diagonalization (BD) Algorithm

1. For $j = 1, \cdots, K$:
    (i) Compute $\tilde{\mathbf{V}}_j^{(0)}$, the right null space of $\tilde{\mathbf{H}}_j$.
    (ii) Compute the SVD:
    $$\mathbf{H}_j \tilde{\mathbf{V}}_j^{(0)} = \mathbf{U}_j \begin{bmatrix} \mathbf{S}_j & \mathbf{0} \end{bmatrix} \begin{bmatrix} \mathbf{V}_j^{(1)} & \mathbf{V}_j^{(0)} \end{bmatrix}^H .$$
2. Use water filling on the diagonal elements of $\mathbf{S}$ to determine the optimal power loading matrix $\mathbf{\Lambda}$ under power constraint P.
3. Set the system modulation matrix as
    $$\mathbf{M}_S = \begin{bmatrix} \tilde{\mathbf{V}}_1^{(0)} \mathbf{V}_1^{(1)} & \tilde{\mathbf{V}}_2^{(0)} \mathbf{V}_2^{(1)} & \cdots & \tilde{\mathbf{V}}_K^{(0)} \mathbf{V}_K^{(1)} \end{bmatrix} \mathbf{\Lambda}^{1/2}.$$
4. The capacity is then
    $$C_{BD} = \max_{\mathbf{\Lambda}} \log_2 \left| \mathbf{I} + 1/\sigma_n^2 \mathbf{S}^2 \mathbf{\Lambda} \right| ,$$
    where the noise variance is σ_n^2 and
    $$\mathbf{S} = \begin{bmatrix} \mathbf{S}_1 & & \\ & \ddots & \\ & & \mathbf{S}_K \end{bmatrix} .$$

For the case of only two receiving users, $\tilde{\mathbf{H}}_1 = \mathbf{H}_2$ and $\tilde{\mathbf{H}}_2 = \mathbf{H}_1$. This is the case considered in the following examples.

4.2 C_{BD} with Respect to $\mathrm{Tr}(\mathbf{V}_1^H \mathbf{V}_2)$

Figure 4.1 shows a scatter plot of the capacity of the BD algorithm (C_{BD}) versus $\mathrm{Tr}(\mathbf{V}_1^H \mathbf{V}_2)$. For this Monte Carlo simulation, $N_R = N_T = 8$ with the two receiving users using 4 antennas each. Here, the trace of $\mathbf{V}_1^H \mathbf{V}_2$ is used to provide a single scalar representation to represent how closely aligned the equal position singular vectors are. With this as our metric, we have

$$0 \leq \mathrm{Tr}(\mathbf{V}_1^H \mathbf{V}_2) \leq N_T.$$

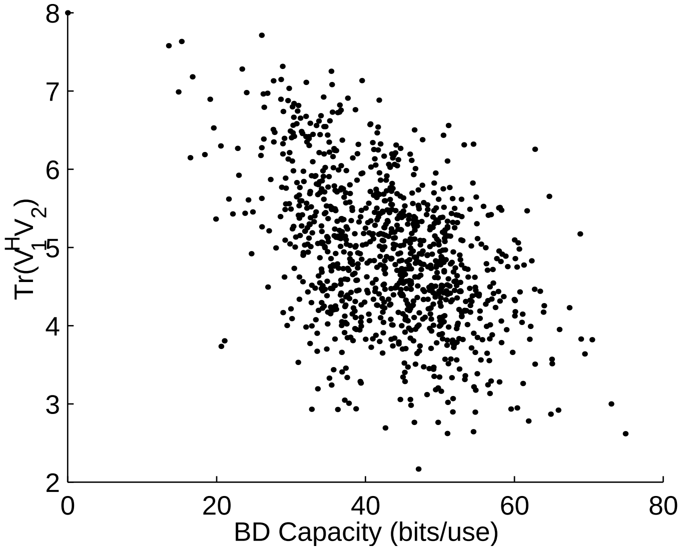

Figure 4.1: Capacity versus $\mathrm{Tr}(\mathbf{V}_1^H\mathbf{V}_2)$

From Figure 4.1 we see that the capacity of the BD algorithm is a weak function of this correlation metric for the case of $N_R \leq N_T$. One might expect that alignment in the right singular vectors between the two receivers would have a stronger effect on the achievable signaling rate. That it only weakly effects the achievable rate can be reasoned from the fact that since $N_R \leq N_T$ here, the block-diagonalization method is able to use a modulation matrix for each user that lies completely in the null space of the other users. In other words, as long as the singular vectors are not completely aligned, there is still a usable null space of $\tilde{\mathbf{H}}_j$ that is a candidate for the modulation matrix $\mathbf{M}_j$.

Not shown here are the results of C_{BD} versus $\mathrm{Tr}(\mathbf{U}_1^H\mathbf{U}_2)$. Simulations showed that the BD capacity is largely independent of this metric. From an examination of the BD algorithm, it is evident that modulation at the transmitter does not depend on the left singular vectors. In fact, since $N_R \leq N_T$ the channel can be block-diagonalized (interference nulled) irrespective of what the left singular vectors are. Each user can then use the same beamformer weights to separate the multiple data streams sent to it without penalty to the sum BD capacity.

The variation in C_{BD} for a given value of $\mathrm{Tr}(\mathbf{V}_1^H\mathbf{V}_2)$ arises from three factors. The first reason is perhaps the most obvious. Normal variations in capacity arise from how well conditioned each channel matrix $\mathbf{H}_j$ is when computing the water filling solution. Second, $\mathrm{Tr}(\mathbf{V}_1^H\mathbf{V}_2)$ weights alignment between the right singular vectors that correspond to the weakest singular values equally with those that correspond to the strongest singular values. It would be expected that correlation among the first singular vectors would have greater effect on C_{BD}. Neither is there any relation to correlation between non-equal position singular vectors. Correlation between these non-equal position singular vectors can effect C_{BD} if they are both in the modulation space to each receiver. Third, there are slightly visible vertical banding effects in Figure 4.1. This is a quantization effect from how many of the singular vectors are aligned so that it becomes unusable for both users. When all are aligned, we see the point in the upper left corner of Figure 4.1 where $C_{BD} = 0$.

4.3 C_{BD} with Respect to New Metric ρ

From the arguments in Section 4.2, we see that $\mathrm{Tr}(\mathbf{V}_1^H\mathbf{V}_2)$ may not be the best metric to use in understanding the effects of singular vector correlation on capacity. Here we will use a new metric defined as

$$\rho = \frac{\mathbf{s}_1^H\mathbf{V}_1^H\mathbf{V}_2\mathbf{s}_2}{\|\mathbf{s}_1\|\|\mathbf{s}_2\|}, \tag{4.1}$$

where $\mathbf{s} = \mathrm{diag}\{\mathbf{S}\}$ and is zero padded to match the size of $\mathbf{V}$. The numerator of equation (4.1) represents a quadratic form in which only the first singular vectors that correspond to non-zero singular values add to the metric. In this manner, we are only comparing the candidate spaces allowable by the BD algorithm for each modulation matrix $\mathbf{M}_j$. This quadratic form also places more emphasis on singular vectors that have greater effect on C_{BD} by multiplying each singular vector with its corresponding singular value. The denominator of (4.1) is a normalization that constrains

$$0 \leq |\rho| \leq 1.$$

This is immediately shown by the Cauchy-Schwarz inequality as,

$$\begin{aligned} |\rho|\|\mathbf{s_1}\|\|\mathbf{s_2}\| &= |<\mathbf{V}_2\mathbf{s}_2, \mathbf{V}_1\mathbf{s}_1>| \\ &\leq \|\mathbf{s_1}\|\|\mathbf{s_2}\| \\ \Rightarrow |\rho| &\leq 1. \end{aligned}$$

Here, $|\rho| = 0$ when $\mathcal{R}\{\mathbf{H}_2^H\} = \mathcal{N}\{\mathbf{H}_1\}$. Put in different terms, this means that the span of the first four singular vectors in $\mathbf{V}_2$ is the same as the span of the last four singular vectors in $\mathbf{V}_1$. From this it immediately follows that the inner products of any of the first four singular vectors in $\mathbf{V}_2$ with any of the first four singular vectors in $\mathbf{V}_1$ is zero, forcing $\rho = 0$.

Figure 4.2 shows a scatter plot of the capacity of the BD algorithm versus $|\rho|$. Here, we again used $N_T = 8$ and $N_{R_j} = 4$. In this figure the vertical banding effects discussed in Section 4.2 are shown more clearly. We also see that C_{BD} is more likely to be lower when $|\rho|$ is close to 1. However, for this case where $N_R \leq N_T$, the achievable rate of the BD algorithm is still weakly affected by correlation in the singular vectors. Once again, this is because unless singular vectors in both $\mathcal{R}\{\mathbf{V}_1\}$ and $\mathcal{R}\{\mathbf{V}_1\}$ are almost exactly aligned, the BD algorithm can still use $\mathcal{N}\{\mathbf{V}_2\}$ of rank 4 to use in $\mathbf{M}_1$.

As discussed in Section 4.2, one of the causes for the variation in C_{BD} is due to the condition of the channel matrix, or in other words multipath richness in the channel. In order to examine the effects ρ has directly on capacity we can normalize the capacity of the BD algorithm by the achievable capacity when all receiving antenna elements are comprised within a signal receiving user, i.e., the 8x8 point-to-point scenario. This latter capacity serves as the maximum attainable for the given channel without the constraint of separate signal processing on each half of the receiving antennas.

Figure 4.3 shows a scatter plot of the normalized capacity versus $|\rho|$. From this figure we still see a weak dependence of capacity on ρ. There are now two possible causes for the variation in normalized C_{BD} for a given value of $|\rho|$. The

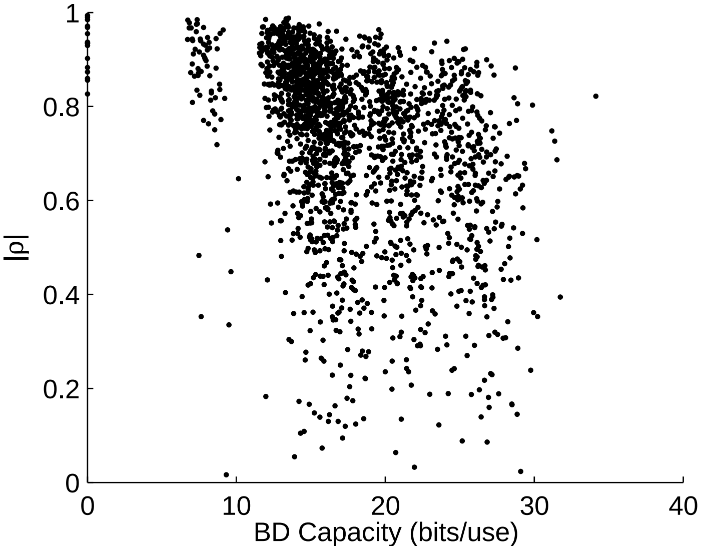

Figure 4.2: Capacity versus ρ

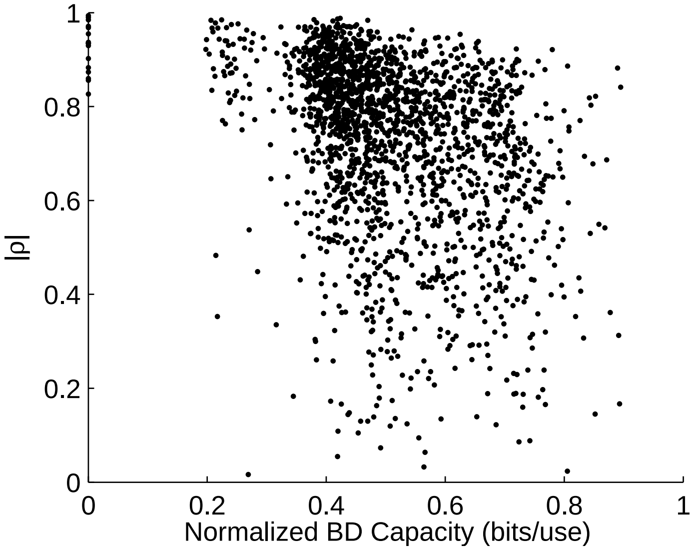

Figure 4.3: Normalized Capacity versus ρ

first is the quantization described earlier that results in a banding effect. The second reason is independent of ρ. It is the variation that arises from receivers separated into groups of antennas that are unable to coordinate with each other as in the single user point-to-point scenario.

4.4 Case 2: $N_R > N_T$

For the case when the total number of receive antennas is larger than N_T, it may still be possible to apply the block-diagonalization method [13]. To be precise, the BD algorithm requires

$$N_T > \max\left\{\mathrm{rank}(\tilde{\mathbf{H}}_1), \cdots, \mathrm{rank}(\tilde{\mathbf{H}}_K)\right\}.$$

The more interesting case, however, is when our channel matrices to each user are full rank or near full rank. Here the block-diagonalization algorithm can only be applied by limiting the number of data streams to each user. It is reasonable that in this case alignment between singular vectors would have a much stronger effect on the achievable rate since it is no longer possible to find a candidate null space of $\tilde{\mathbf{H}}_j$ to use for $\mathbf{M}_j$. In this case, alignment in the singular vectors should also have a greater negative effect on theoretical capacity. For example, if the right singular vectors are fully correlated, then the transmitter can no longer distinguish between the two users and must then divide the rank($\mathbf{H}_j$) available data streams between the two users. If the right and left singular vectors are completely uncorrelated, there is full flexibility in finding a good solution to maximizing the sum capacity. Determining the capacity regions for more general approaches to maximizing the sum capacity is still an area of needed research.

4.5 Chapter Summary

This chapter focused on the block-diagonalization algorithm to show representative results on how alignment between singular vectors might impact MIMO transmission performance. The block-diagonalization method was summarized to allow free discussion on its reliance upon the right singular vectors corresponding to each receiving user. The capacity of the BD method C_{BD} was compared to two different scalar correlation metrics and the use of each was detailed. Since the BD algorithm guarantees for $N_T \geq N_R$ that the null space of the channel matrix of one user is large enough to support transmission to the other user, C_{BD} was only greatly effected for high correlation values. Within the chapter was also explained why this lead to “banding” effects in C_{BD}. The chapter concluded with a discussion of the $N_R > N_T$ case.

Chapter 5

MIMO Measurement Platform

To assist in conducting this research, an existing 16-channel transmit chassis and an existing receive chassis were made available [7]. These systems are able to perform narrowband channel measurements with a radio frequency (RF) of 0-3 GHz. If full stationarity is assumed, then this single receiver could be used to take measurements at different locations to statistically analyze the channel matrix as if they were taken simultaneously. In general, wireless channels are time varying and this method is valid only in ideal circumstances. Furthermore, for the statistics of interest here, a good distribution of sampled channels is necessary. In terms of the two ring channel model, we want a large number of Monte Carlo realizations. To attain this, it is convenient to take measurements of a changing wireless channel with two receivers at the same time. Otherwise, many time consuming experiments must be performed with a single receiver measuring different realizations of statistically similar channels. This is the motivation for second receive system constructed as part of this research.

5.1 Hardware Design and Construction

The new receive system was designed to be easily incorporated into the existing narrowband measurement platform. This meant that it needed to operate over the same frequency range, implement the same type of data storage, and have similar receiver gain response characteristics. The new system also needed to be fabricated with minimal cost. The following list summarizes the key requirements of the new receive system:

Functional specifications:

1. *Compatibility.* The new receiver must be fully compatible with the existing measurement collection hardware. This includes the following items:
    - *Frequency Range.* The system should be able to operate at a carrier frequency of 1-3 GHz, an intermediate frequency (IF) of 25 kHz, and a data rate of 12.5 kbits/s.
    - *Amplification.* RF and IF amplifiers should be chosen to allow operation at nearly the same signal levels of the existing receiver.
    - *Data Acquisition.* Data should be acquired and stored in a manner to be compatible with the existing receiver.
2. *Development.* The system was to be built using the available tools at Brigham Young University and development time should be minimized.
3. *Cost.* The new receiver should use available components already purchased when possible. New components should be limited in cost.
4. *Stability and Robustness.* The new receiver should have a stable response and calibration. It should be able to withstand shocks and regular use, including connection and reconnection of modular parts and cables.

Figures 5.1 - 5.8 show the hardware and corresponding schematics resulting from this development, including the full receive system on its cart, the receive chassis with installed components, the backplane, IF Board, and a RF receive card. Included here are only items with a different design than the existing hardware.

The easiest and best way to achieve all the goals described by the functional specifications list was to begin with the existing receiver design in building the new receiver. However, there were some aspects of the design for the original systems that needed improvement.

AT switching power supplies can be quite noisy and require high frequency filtering to be useful for a receive system. To mitigate this effect, the new receiver employs a linear power supply instead of a switching power supply.

Another improvement was the use of PC-type SMA connectors on the broadband backplane. These are connectors that penetrate the board and solder to the back side providing more mechanical rigidness in the connection. The surface mounted SMA connectors used on the original receiver backplane were fragile and tended to break off or contribute to changed calibration results between different sets of measurements. In order to use the PC-type SMA connectors, the transmission line that divided the local oscillator (LO) to the different RF receive cards needed to be put on the reverse side of the backplane (see Figures 5.3 and 5.4). This meant that the transmission lines on the receive cards also needed to be changed so that it would match up to the connections on the backplane (see Figure 5.5).

On the new receive cards, the amplifiers were biased so as to operate within the specifications of the manufacturer. This allowed for more stability in the operating characteristics of the new receiver. This bias scheme is shown in the new schematic for the receive cards in Figure 5.6. This was also convenient since it allowed the entire system to operate at +/- 12 Volts (this is the voltage supply level that the IF board required as well) which meant a single linear voltage supply could be used.

Soldered vias to equalize potential between the ground planes of the grounded coplanar waveguide (GCPW) boards were increased in number and packed more tightly. This was performed to reduce power leakage between the RF and LO from waveguide effects through the card. The hundreds of vias were filled with solder paste which is baked to form a solid crystalline conductive structure. Figures 5.4 and 5.5 show the vias around the transmission paths for both the backplane and RF cards.

In order to accommodate the same method of data storage, the same data acquisition board was used as well as the same programmable opamps and anti-aliasing filters on the IF board. The IF board and schematic are shown in Figures 5.7 and 5.8. For more detail on the existing hardware elements not elaborated on in this section, the reader is referred to [7].

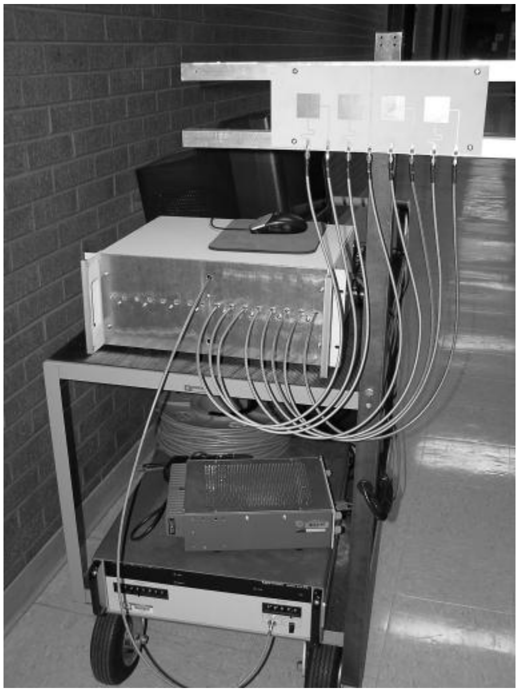

Figure 5.1: Full new receiver system

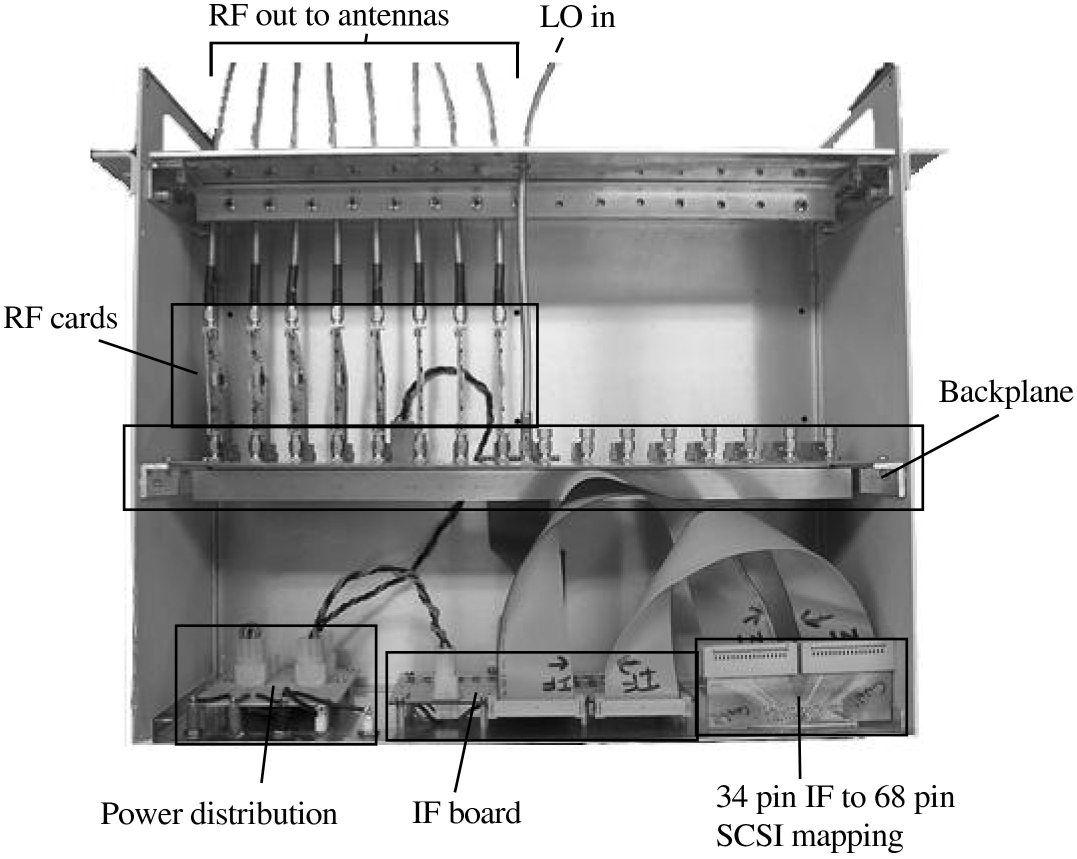

Figure 5.2: Custom RF receive chassis

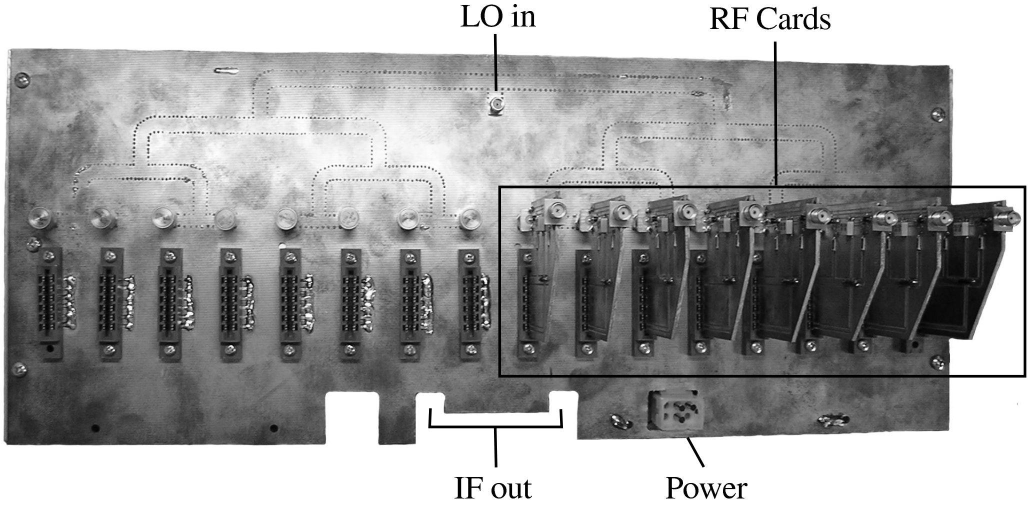

Figure 5.3: Backplane front side

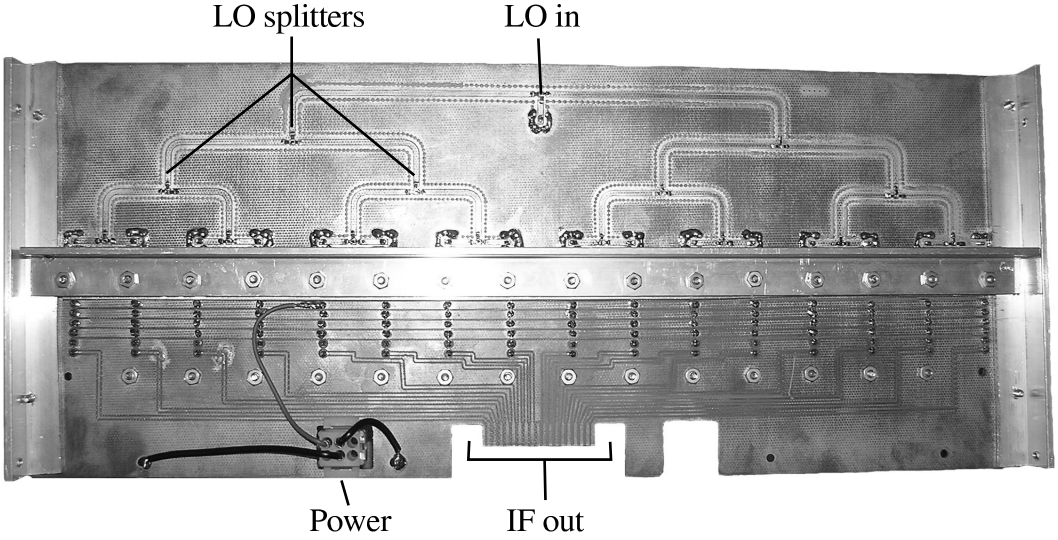

Figure 5.4: Backplane reverse side

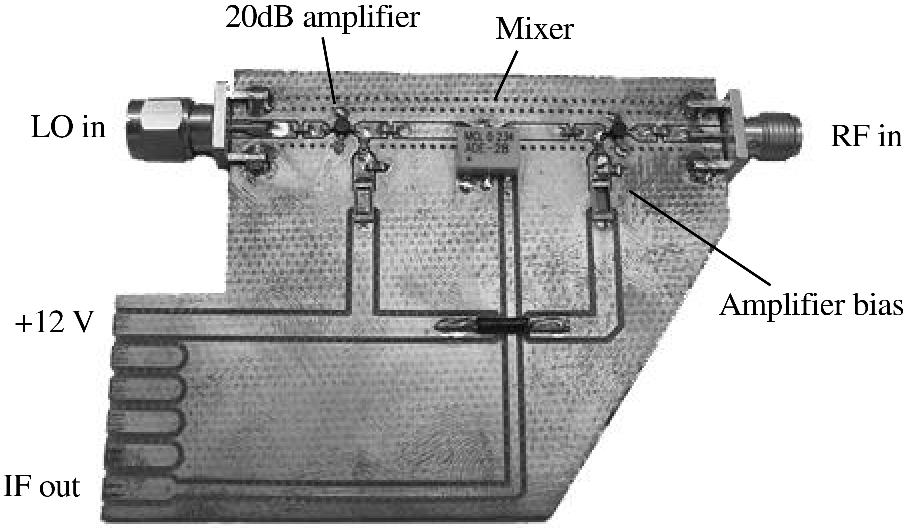

Figure 5.5: RF receive card

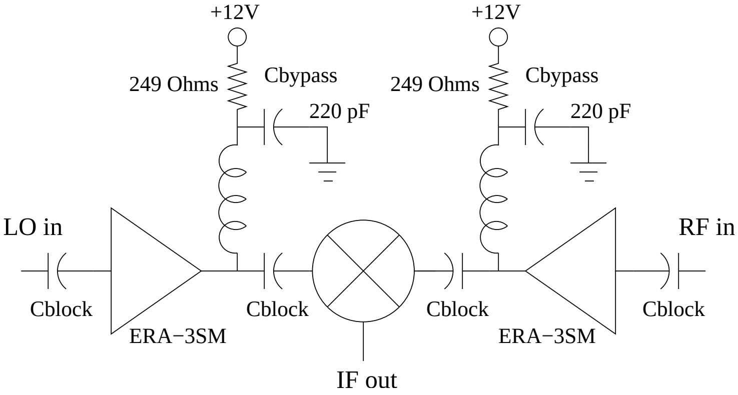

Figure 5.6: RF receive card schematic

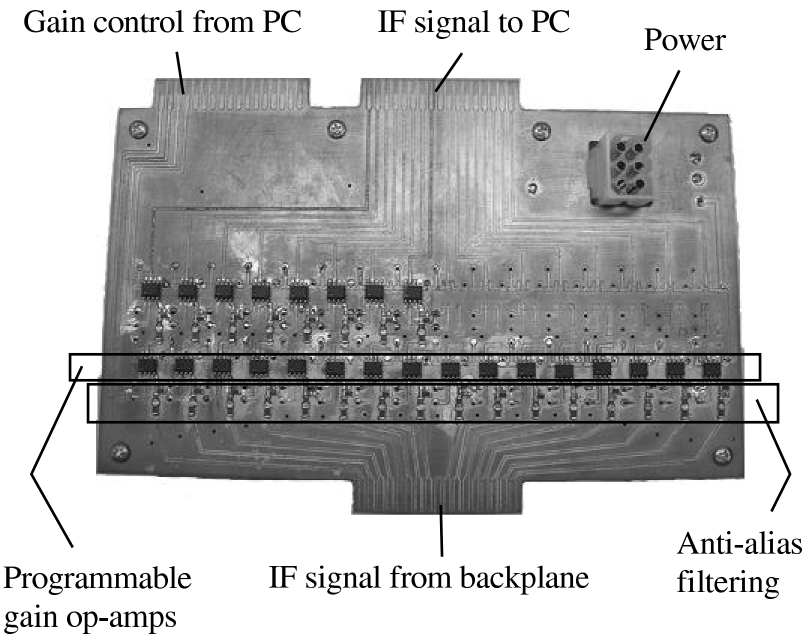

Figure 5.7: IF Board

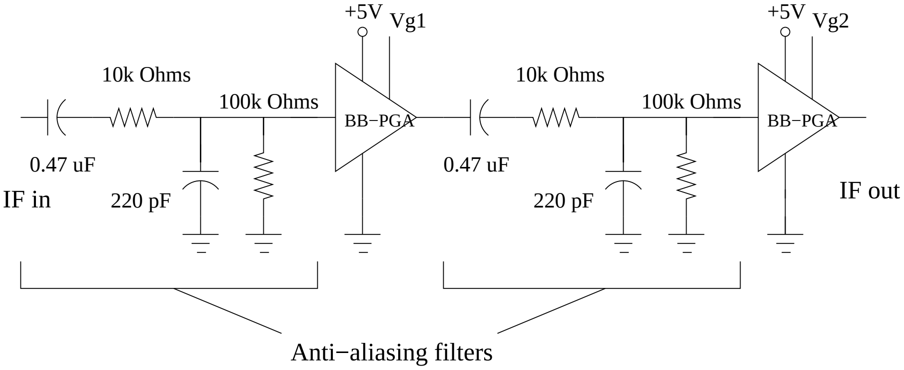

Figure 5.8: IF Board schematic

5.2 Signal Processing

During actual measurements, the receivers simply sample the raw IF waveforms and store this as raw data. Afterward, the signal processing is performed at the receivers as post-processing. The basic steps of this signal processing is diagrammed in Figure 5.9. Details on this processing appear in [7].

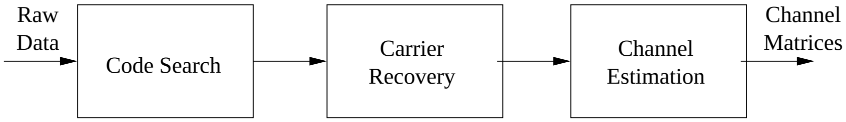

Figure 5.9: Signal processing block diagram

5.2.1 Existing Work

Originally, the preexisting measurement platform transmitted N_T different binary phase shift keyed (BPSK) pseudo-random codes. This meant that during the code search phase of signal processing, the proper alignment of the codewords needed to be determined within interfering transmitted codewords. In order to determine the proper alignment (symbol timing), the raw data from one receive channel is despread, and one transmitted symbol stream is recovered from the data. The despread signal is then used to perform carrier phase and frequency recovery. This method of symbol timing and carrier phase recovery with MIMO systems works adequately for long pseudo-random codewords. However, these long codewords constrain the time resolution of the channel probing to be poor. Also, the post-processing to perform these tasks was computationally intensive. For the 1000 symbol length codewords used at a bit rate of 12.5 kbits/s, the time resolution is

$$t_{res} = 1000 \text{ bits} \times \frac{1 \text{ s}}{12.5 \text{ bits}} = 8 \text{ ms}.$$

For more information on this preexisting signal processing work for the MIMO measurement system, refer to [7].

5.2.2 New Tx Code Stream: Short Codes

In order to improve on both the time resolution and reliability of MIMO channel estimation, a new method of signal processing was developed that makes use of new shorter code streams. Since this new method isn't included in the published literature, it will be discussed briefly here.

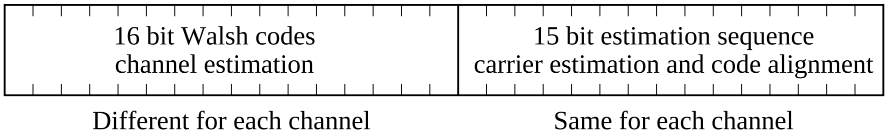

Figure 5.10: New Tx short codes

Figure 5.10 diagrams the new short codes. These short codes are 31 bit binary sequences for BPSK transmission. The first 16 bits are generated from orthogonal Walsh codes and are used to estimate the channel. The last 15 bits are the same for each channel and were chosen to have nice autocorrelation properties to allow for good despreading. These last 15 bits are used to perform code alignment, frequency and phase estimation, as well as symbol timing recovery. The signal processing for the short codes follows the same basic steps shown in Figure 5.9.

Code Alignment. As before, the code alignment is determined by despreading the signal from the strongest receive channel. If we multiply the received signal against a properly aligned codeword for uncorrelated code sequences, the discrete Fourier transform (DFT) exhibits a peak at the center frequency of the IF signal. For the short codes, the despreading portion of the signal processing is the same as that described in [7].

Frequency Estimation. With the despread signal in hand, the last 15 bits of the codeword can be masked to perform carrier recovery using the square law. As discussed, the DFT of the strongest receive channel multiplied with itself exhibits a strong peak at the actual IF from which the frequency can be estimated. Usage of just the last 15 bits in this estimation allows the carrier frequency recovery to be performed without interference due to the other codewords since this portion is the same across all transmit channels. The phase can be normalized to the phase of H_{11} for finer tuning. This method of carrier frequency estimation is much faster than the previous method used on the pseudo-random codes where a full correlation to all possible IFs was performed.

Symbol Timing and Channel Estimation. Once the frequency is estimated, the received streams are then converted to baseband where normal baseband signal processing techniques can be used on the last 15 bits of the codewords for symbol timing recovery. Maximum Likelihood channel estimation of $\mathbf{H}$ is then performed using the first 16 bits containing the orthogonal Walsh codes. The data is sent at a bit rate of 12.5 kbits/s. This gives a time resolution in channel probing of

$$t_{res} = 31 \text{ bits} \times \frac{1 \text{ s}}{12.5 \text{ bits}} = 2.48 \text{ ms}.$$

5.2.3 Timing Synchronization Between Receivers

Each receiver separately performs carrier phase and symbol timing recovery for the transmitted BPSK signals. However, for a time varying channel, it is necessary to be able to match up the timing of the measurement sets between the two receivers. In this manner, the same channel realization is being compared for statistical accuracy. A simple method for doing this is to synchronize the operating system clocks of the two receivers and have them start taking measurements at the same time. This method may be adequate for a slow varying channel. It was observed that over a period of a few hours, the two system clocks could vary on the order of a second. A new, but also simple method was devised to ensure that measurements could be synchronized in time so that similar channel realizations are compared during post processing. A 10 Hz square wave signal from a single frequency generator was sent along equal length cables directly to the digitizing card of each receiver. The two data sets were then easily finely matched in time during post-processing to the rise of the pulse. This approach allows the computer clocks to drift up to 1/10 second apart while taking measurements, and still have full synchronization. The disadvantage of this method is the requirement of a cable tethering the two receivers.

5.3 Chapter Summary

This chapter described the new receiver hardware constructed to extend the capabilities of the existing MIMO measurement platform. A quick overview of the signal processing performed to estimate the channel matrix using new transmitted short codes was given. Finally, an implementation method of synchronizing the measurement timing between the two receivers was described.

Chapter 6

Data Collection Results

In this chapter data collected with the MIMO measurement hardware discussed in Chapter 5 is presented. Different experiments were performed in a number of important scenarios to analyze effects of rich indoor and sparse outdoor environments on singular vector correlation. Each section of this chapter describes a different experiment, including the results and conclusions drawn.

6.1 Experiment A

6.1.1 Measurement Location and Parameters

In the first data collection experiment, indoor measurements were performed on the fourth floor of the Clyde Building at Brigham Young University at night. Table 6.1 shows the measurement configurations for this experiment. This carrier frequency

Table 6.1: Measurement parameter for Experiment A

Parameter	Value
Distance between sets	5 ft
Length of sets	20 seconds
Carrier frequency	2.47 GHz
IF frequency	25 kHz (nominal)
Bit rate	12.5 kbits/s
Tx array	8 monopoles
Rx arrays	4 dual polarized patches

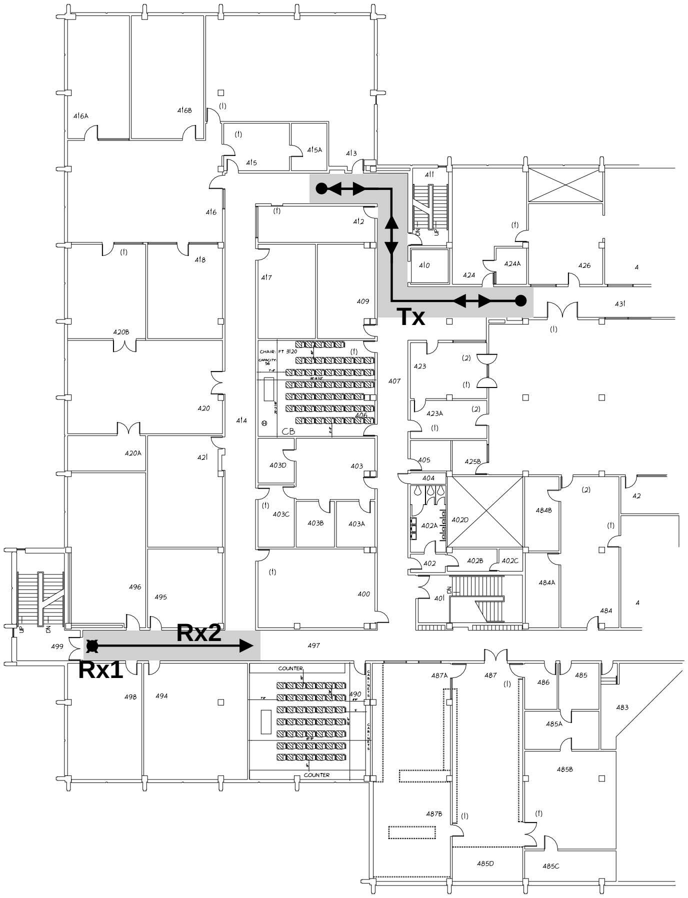

Figure 6.1: Experiment A locations and paths

was chosen to move away from the uplink and downlink frequencies of wireless access points located in the building. The access point frequencies were then out of band and were filtered by the anti-aliasing filters on the IF board. The desired signal received power was measured to be at least 45dB greater at the receiver than the signal strength of the wireless LAN when operating. The effect of the wireless LAN signal can therefore be considered negligible on the results of the measurements.

Figure 6.1 shows the location of the transmitter and the two receivers for this experiment. Rx1 remained at the location nearest the stairwell throughout the measurements while Rx2 was moved in 5 ft increments along the path shown. Both antenna arrays were directed toward the path taken by Rx2. The transmitter was continuously moved along the path shown for each measurement set taken.

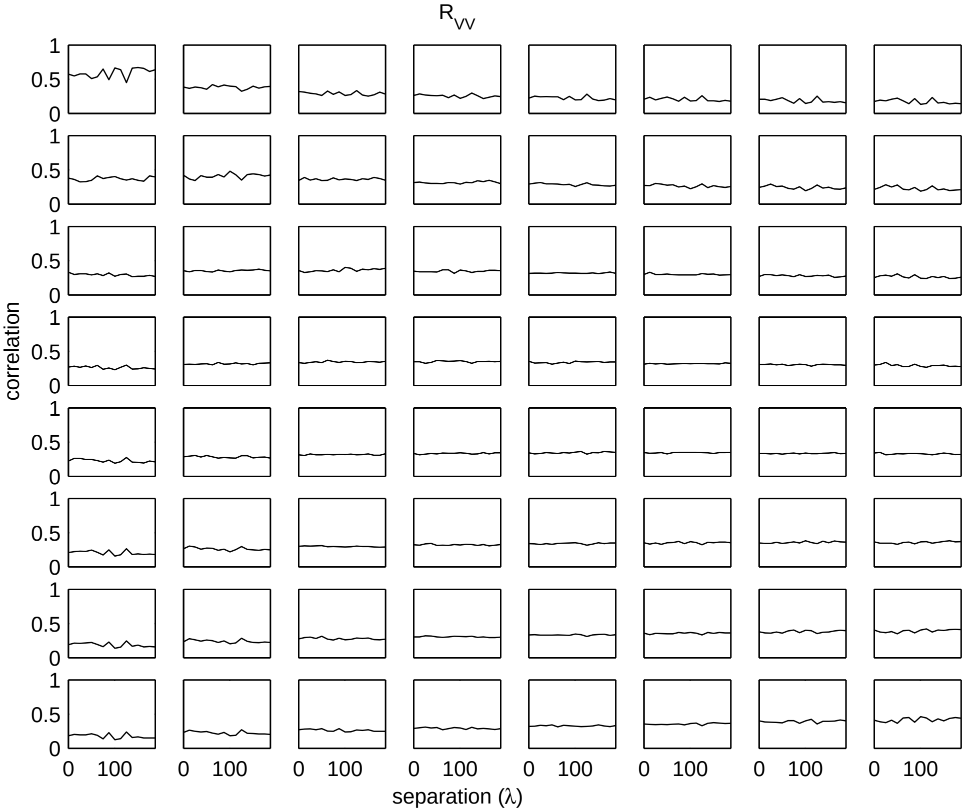

Figure 6.2: Alignment between right singular vectors. Experiment A, 8×8 MIMO.

6.1.2 Processed Data Results

Figure 6.2 shows the results for correlation in the right singular vectors, while Figure 6.3 shows the same for the left singular vectors. As in the simulations performed in Chapter 3, these are plots of the magnitude of each element of $\mathbf{R_{VV}}$ and $\mathbf{R_{UU}}$ with respect to receiver separation in wavelengths. In these results, we can see correlation figures that are much stronger than for the i.i.d. Gaussian case, which from the 8×8 case in Table 3.1 are 0.1013 for each element in $\mathbf{R_{VV}}$ and $\mathbf{R_{UU}}$. Also notice that the correlation figures do not vary significantly with receiver separation. This behavior can be explained by the very rich scattering environment for this indoor channel, resulting in an independent scatterer configuration seen by each receiver. This result closely follows that Section 3.2.2 where each has its own independent ring of scatterers. See Figure 3.7 and 3.8 for a comparison.

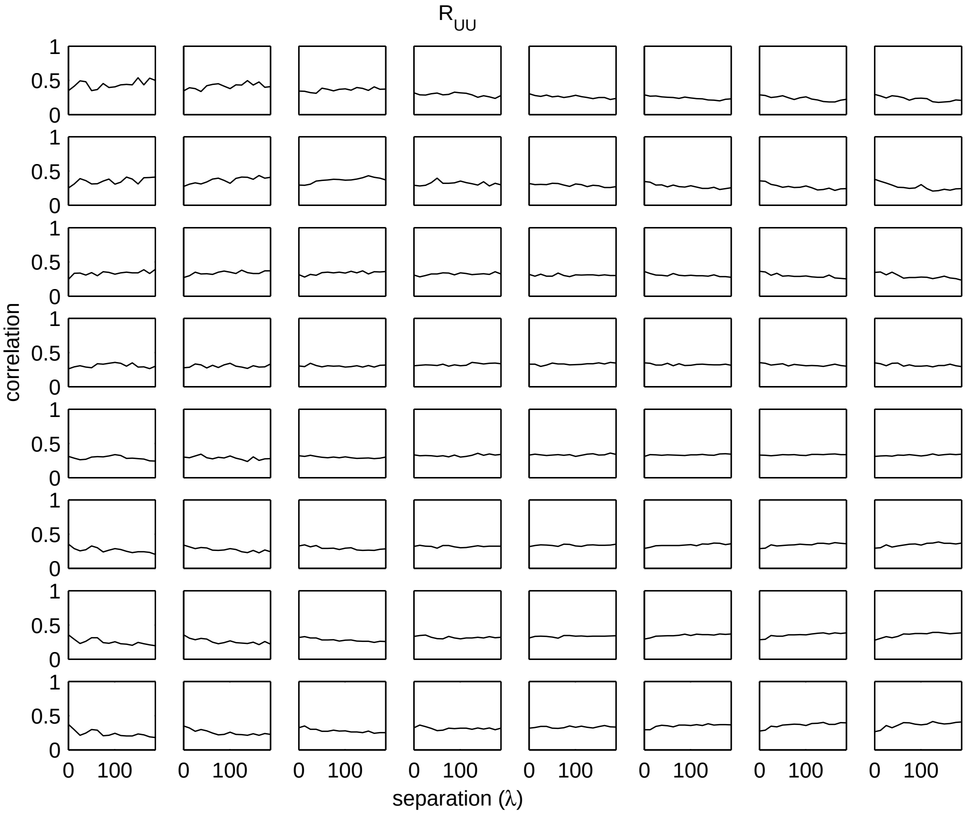

Figure 6.3: Alignment between left singular vectors. Experiment A, 8×8 MIMO.

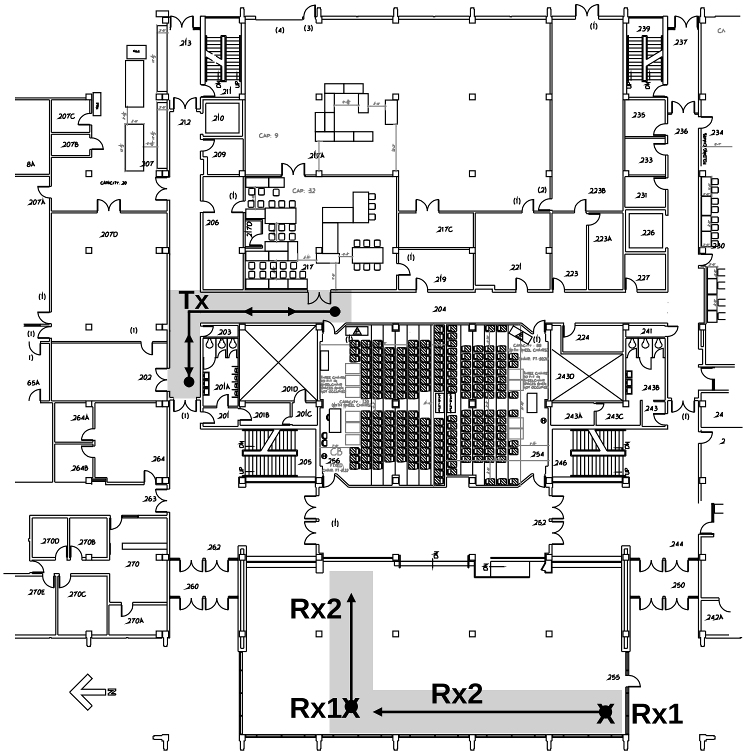

Figure 6.4: Experiment B locations and paths

6.2 Experiment B

6.2.1 Measurement Location and Parameters

This experiment was performed on the second floor of the Clyde Building at Brigham Young University during the night. Figure 6.4 shows the locations for the transmitter and two receivers. The measurement parameters are the same as for Experiment A shown in Table 6.1. Two different scenarios were performed for this experiment as shown in Figure 6.4. During each set of measurements, the transmitter was moved along the path shown in the figure. Rx1 remained stationary while Rx2 moved along each of the two paths shown. This location for Experiment B was chosen to simulate a more open indoor environment. The transmitter path was chosen to provide a wide variety of different transmit scattering environment realizations for each measurement set. This provides a better statistical sampling that is averaged at each set location (separation distance). The motivation behind the receiver location

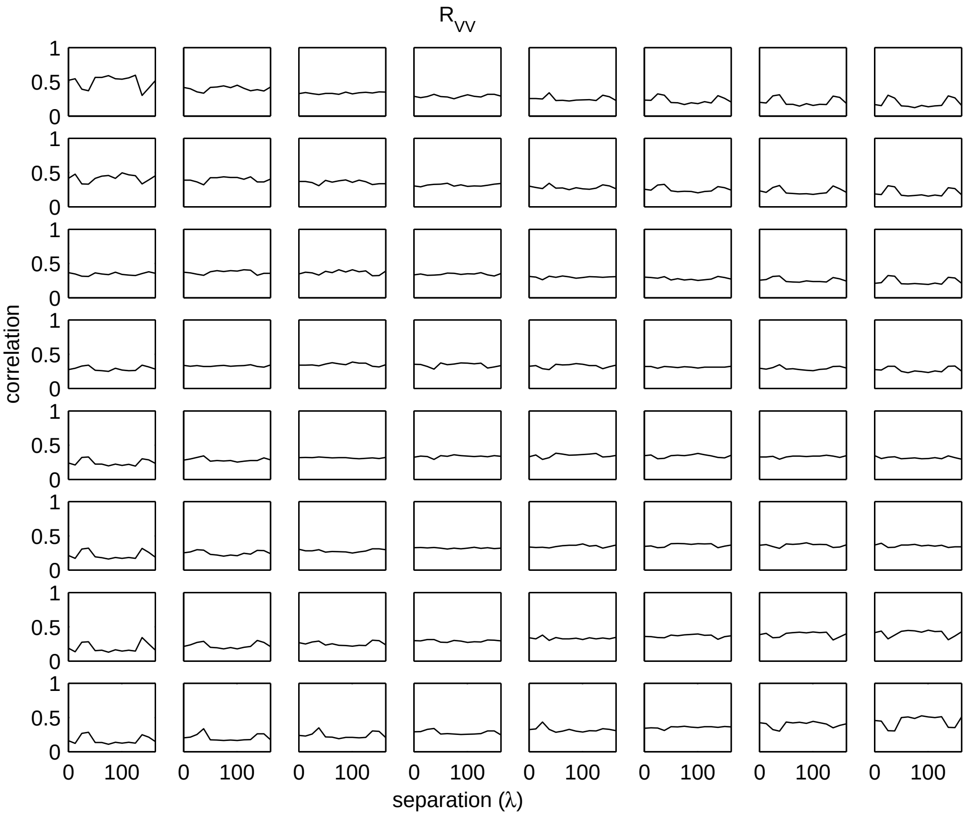

Figure 6.5: Alignment between right singular vectors. Experiment B.1, 8×8 MIMO.

was to measure an environment where the two receivers might see the same local scatterers. Thus, the two ring model where the same ring is employed for both scatterers was hoped to suit this experiment. However, as will shortly be shown in the results, the measurements showed that the model that better fits this situation was that using independent rings.

6.2.2 Processed Data Results

Figure 6.5 shows the results for correlation in the right singular vectors for the horizontal right to left path in Figure 6.4, while Figure 6.6 shows the same for the left singular vectors. The results for the vertical path are shown in Figures 6.7 and 6.8. Although the two receivers were located in the large lobby of the Clyde Building, it is evident from these results that the alignment in the singular vectors is fairly constant

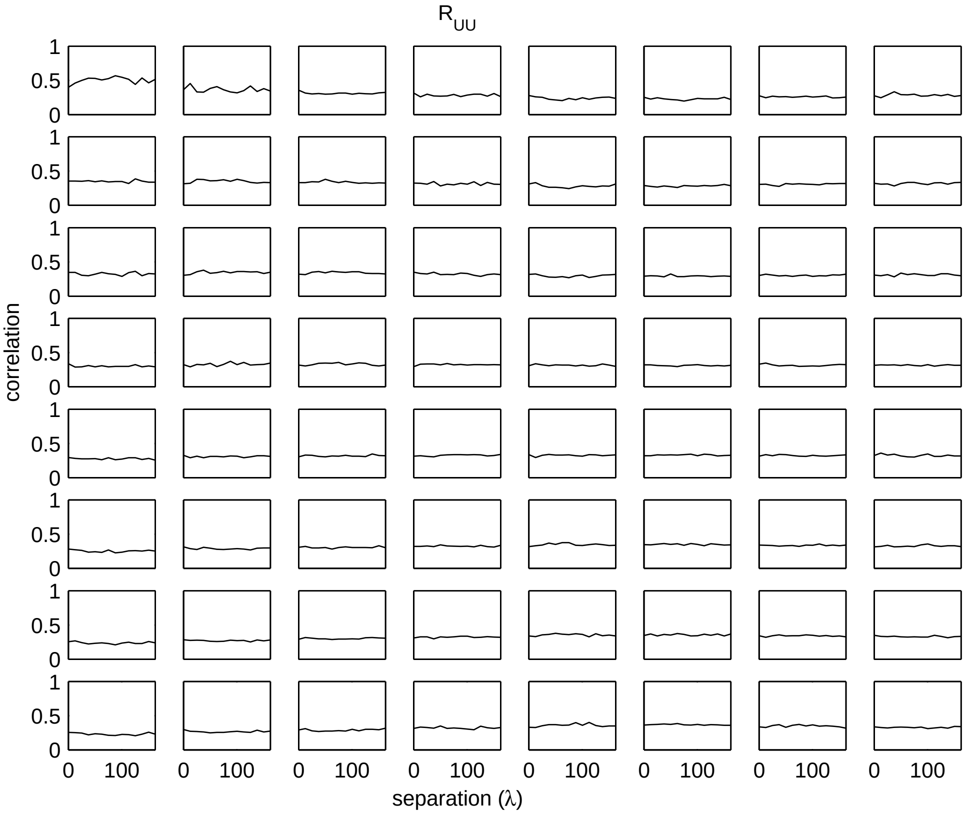

Figure 6.6: Alignment between left singular vectors. Experiment B.1, 8×8 MIMO.

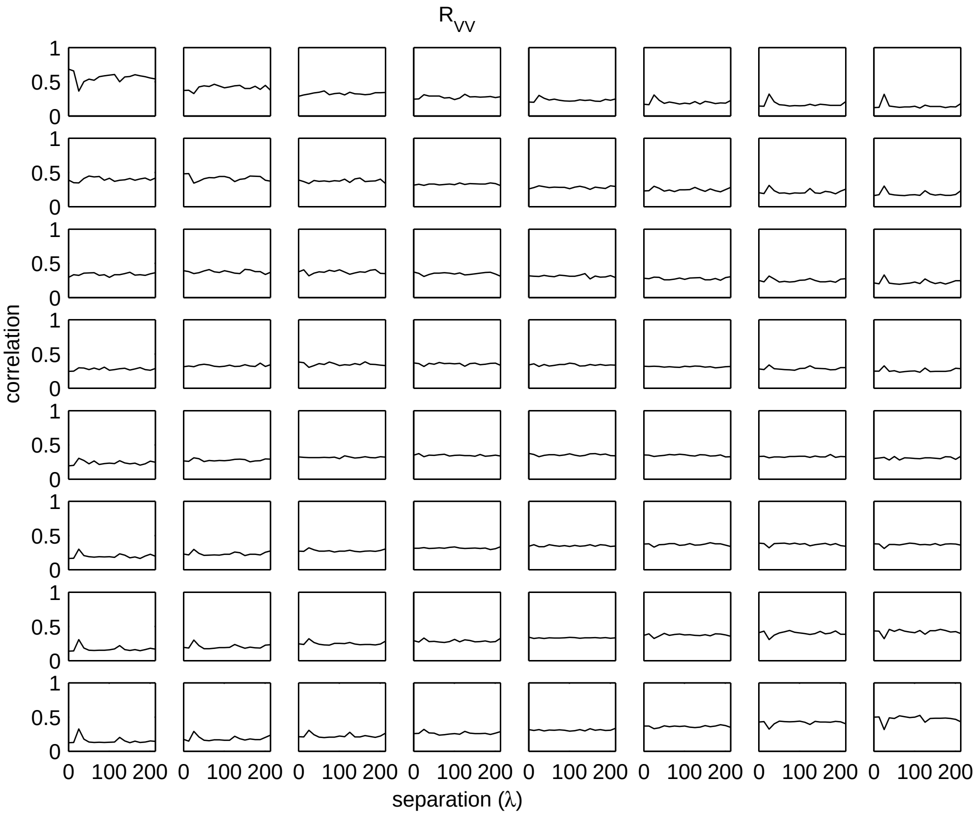

Figure 6.7: Alignment between right singular vectors. Experiment B.2, 8×8 MIMO.

with respect to separation distance. This indicates that the receivers see independent corresponding scatterers and that there exists a rich scattering environment even in this large open lobby. What is interesting to note is that $\mathbf{R_{VV}}$ shows slightly closer alignment for equal position singular vectors than $\mathbf{R_{UU}}$. This suggests that the two receivers are interacting with fairly similar transmit scatterers as in the simulations performed in Chapter 3. However, both $\mathbf{R_{VV}}$ and $\mathbf{R_{UU}}$ show greater correlation for this collected data than in the simulation performed in Section 3.2.2. The source of this increased correlation is unclear, but may be due to a number of factors such as a nonuniform distribution in angle of scatterers and a scatterer amplitude distribution that is not complex normal.

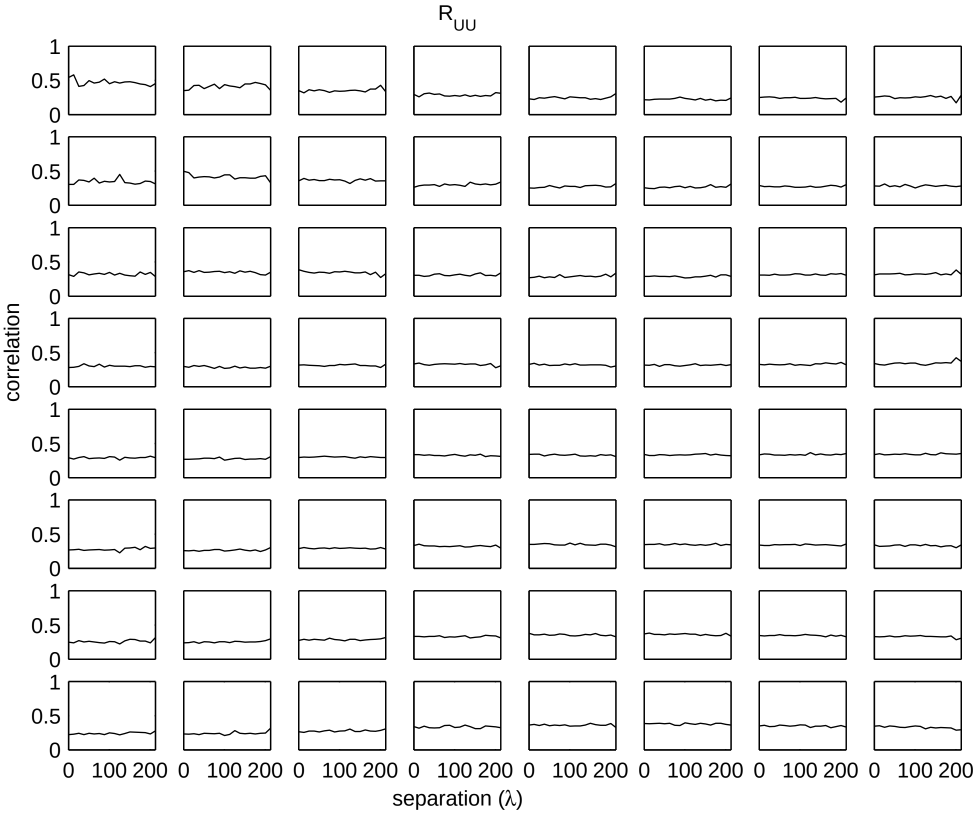

Figure 6.8: Alignment between left singular vectors. Experiment B.2, 8×8 MIMO.

Table 6.2: Measurement parameter for Experiment C

Parameter	Value
Distance between sets	Continuous
Length of sets	30 ft in 30 seconds
Carrier frequency	2.45 GHz
IF frequency	25 kHz (nominal)
Bit rate	12.5 kbits/s
Tx array	4 dual polarized patches
Rx array	4 dual polarized patches

6.3 Experiment C

6.3.1 Measurement Location and Parameters

The measurements for this experiment were collected by Jon Wallace. These measurements were performed in the Deseret Towers field by the Harmon Building at Brigham Young University. For this experiment, only one receiver was used and it will be assumed that the channel is stationary throughout each measurement set. Figure 6.9 shows the location of the transmitter and receiver while Table 6.2 gives the measurement parameters for this experiment. The receiver was moved continuously while taking measurements for a total distance of 30 ft in 30 s (1 ft/s). This measurement was duplicated and the two sets were averaged to obtain the correlation results.

6.3.2 Processed Data Results

Figures 6.10 and 6.11 show the correlation results for the right and left singular vectors respectively. Note that this is effectively one channel realization since the transmitter remained in the same location and the channel is assumed stationary throughout each set. For this reason, these figures show a large variance in the inner product of the singular vectors. Still, looking at the correlation results for a single channel realization is telling since it shows how much variation we might expect to see in this correlation for a given realization. We can see that in this channel,

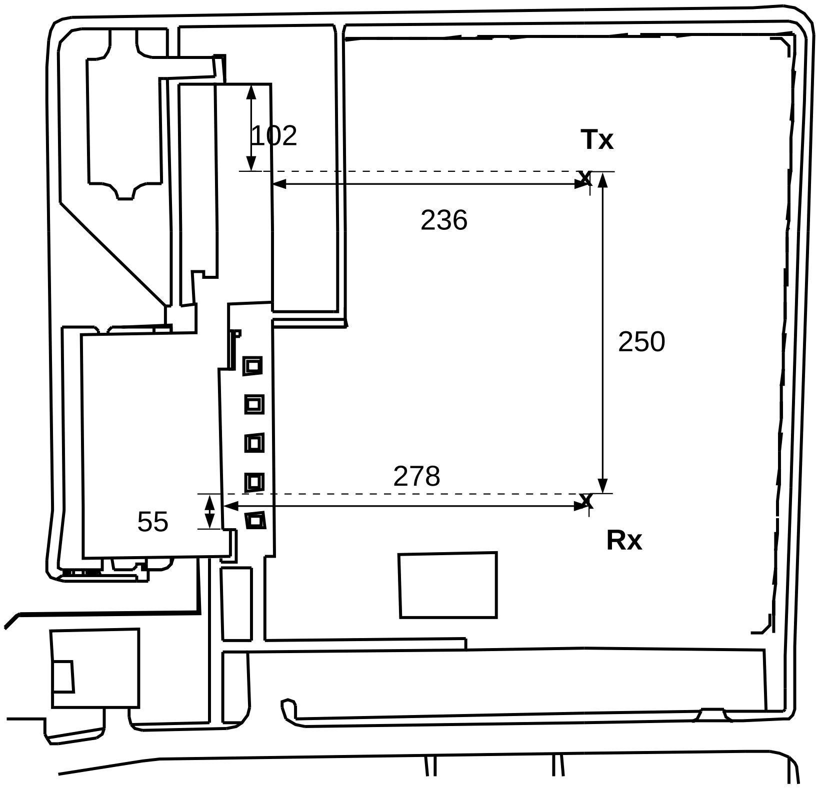

Figure 6.9: Experiment C, D locations and paths. Distances given are in feet.

the first four singular vectors remain highly correlated throughout the measurement sets. We can also notice more alignment between the right singular vectors than the left. This measurement corresponds well with the simulation performed with a small number of scatterers. This is intuitively pleasing since the measurement was taken in a sparse scattering outdoor environment. The difference between these results and those simulated in Section 3.2.2 are that $\mathbf{R_{UU}}$ here shows greater correlation. Recall from Section 3.2 that the values in Figure 3.12 converge to same results obtained when simulating different scattering rings for each receiver.

Since this experiment represents a single channel realization where transmission is in a field and dominant scattering is off a nearby building, it is revealing to look at the eigenbeams of the channel for at least two different receiver locations. Figures 6.12 - 6.15 show these transmit and receive eigenbeams. From these figures it is evident why we see such strong correlation in the first four singular vectors in Figures 6.10 and 6.11. As expected, this strong correlation results in similar eigenbeamformers. Note also how these beamformers correspond to the map of Figure 6.9. We see that in forming the eigenbeams, the transmitter effectively bounces most of its power off the main scatterer which is the building shown in the figure. Likewise, the receiver applies its eigenbeamformer to receive the signal from this dominant scatterer. The reason for strong correlation in the first four singular vectors is most likely due to subdominant scatterers that remain similar throughout the receiver's movement.

6.4 Experiment D

6.4.1 Measurement Location and Parameters

This conglomeration of measurements was also collected by Jon Wallace in the Deseret Towers field. The parameters are the same as shown in Table 6.2 for Experiment C and the location the same as in Figure 6.9 except that in this case each set represents different antenna types (monopole and dual polarized patch), different array orientations, and different receiver paths. These are cataloged in Table 6.3. The directions shown in the table are the same as in Figure 6.9, where up is north.

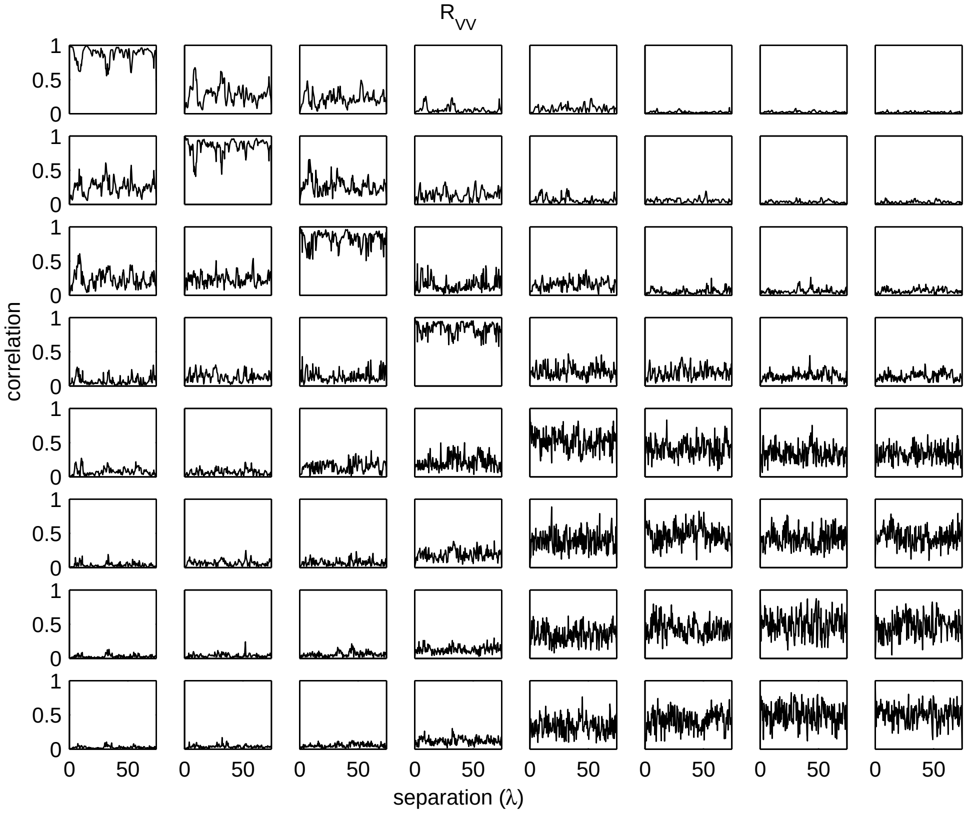

Figure 6.10: Alignment between right singular vectors. Experiment C, 8×8 MIMO.

Table 6.3: Measurement orientations and paths

Set #	Ant. Type	Tx Orient.	Rx Orient.	Rx Path
1	Patch	←	←	↓
2	Patch	←	↓	→
3	Patch	↑	←	↓
4	Patch	↓	↑	←
5	Monopole	→	←	←
6	Monopole	→	←	←
7	Monopole	↑	↓	↓
8	Monopole	↑	↓	↓

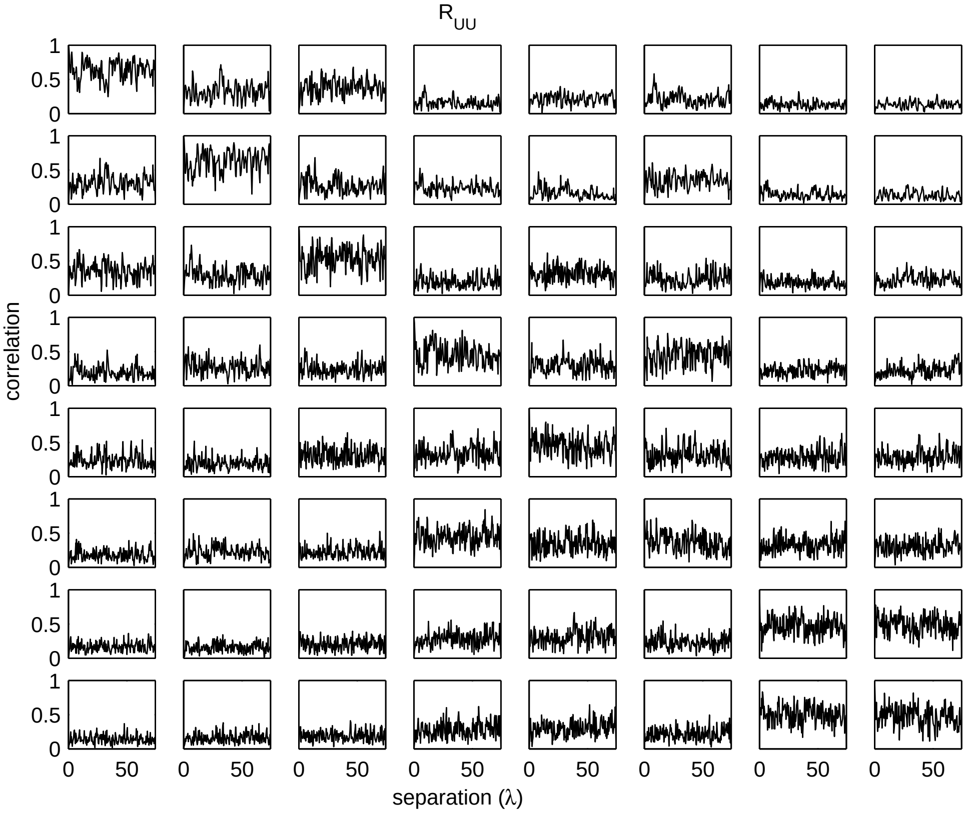

Figure 6.11: Alignment between left singular vectors. Experiment C, 8×8 MIMO.

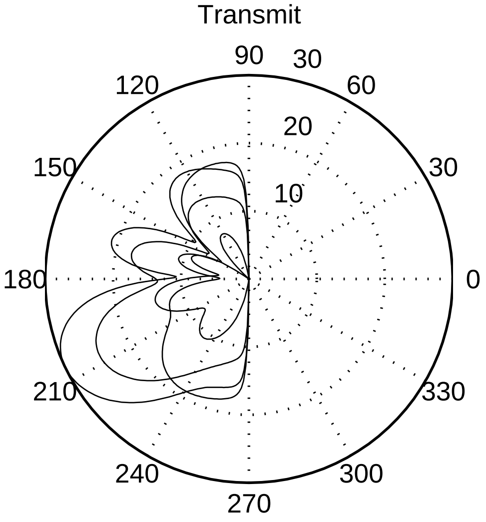

Figure 6.12: First four Tx eigenbeams. Rx in original location. Experiment C.

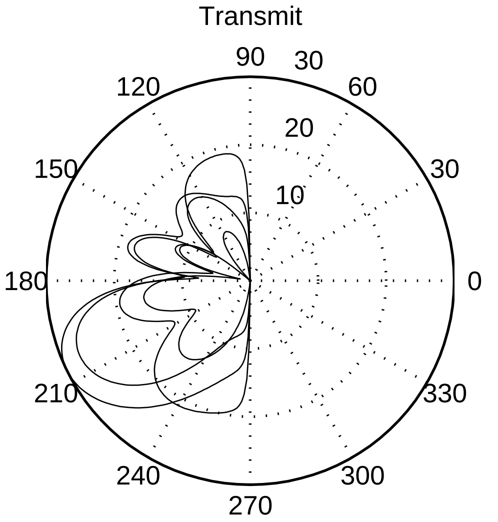

Figure 6.13: First four Tx eigenbeams. Rx moved 9 ft. Experiment C.

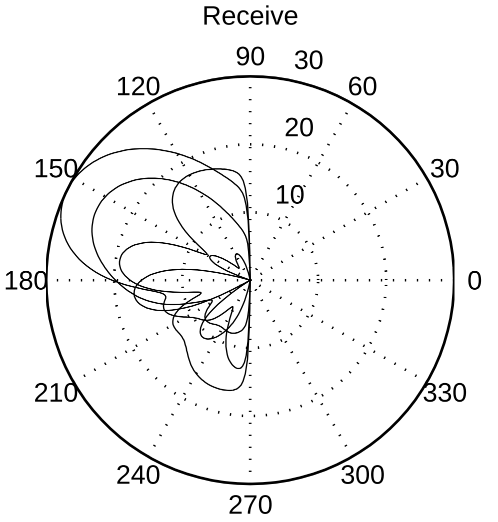

Figure 6.14: First four Rx eigenbeams. Rx in original location. Experiment C.

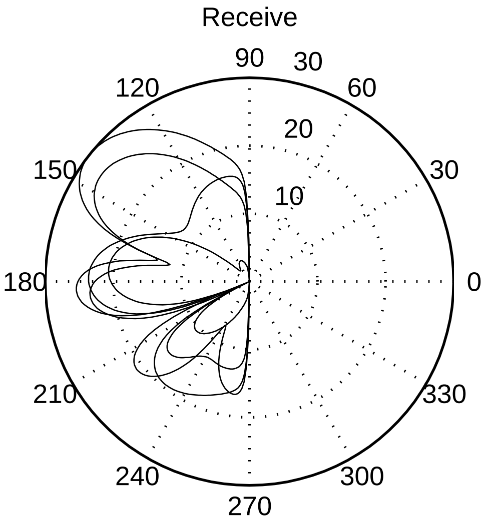

Figure 6.15: First four Rx eigenbeams. Rx moved 9 ft. Experiment C.

6.4.2 Processed Data Results

Figures 6.16 and 6.17 show the results for the inner product of the right and left singular vectors respectively. This data is the average from all the different scenarios given in Table 6.3. These results present a more statistical representation of what the MIMO channel environment in an open field with a nearby building might look like. Here we see more roll off in the correlation of equal position right singular vectors than Figure 6.10. This is because we are averaging the effects of scenarios that include a LOS path (which leads to very strong correlation in the first singular vectors) with other non-LOS scenarios that incorporate a slightly richer scattering environment.

6.5 Chapter Summary

Two separate indoor experiments conducted showed representative results of rich indoor environments. Although one experiment was conducted with the receivers in a large lobby and the other in a narrower hallway, they both statistically showed the same results. The correlations in $\mathbf{R_{VV}}$ and $\mathbf{R_{UU}}$ were independent of receiver separation distance. In view of the two ring model, this implies that the scatterers

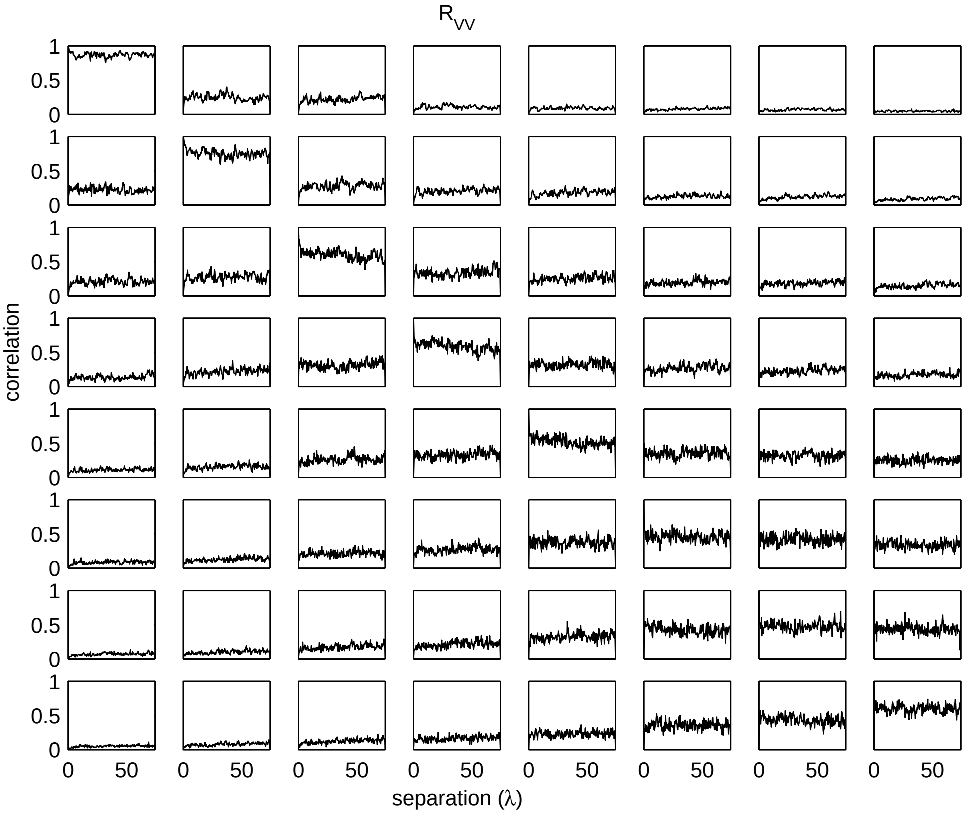

Figure 6.16: Alignment between right singular vectors. Experiment D, 8×8 MIMO.

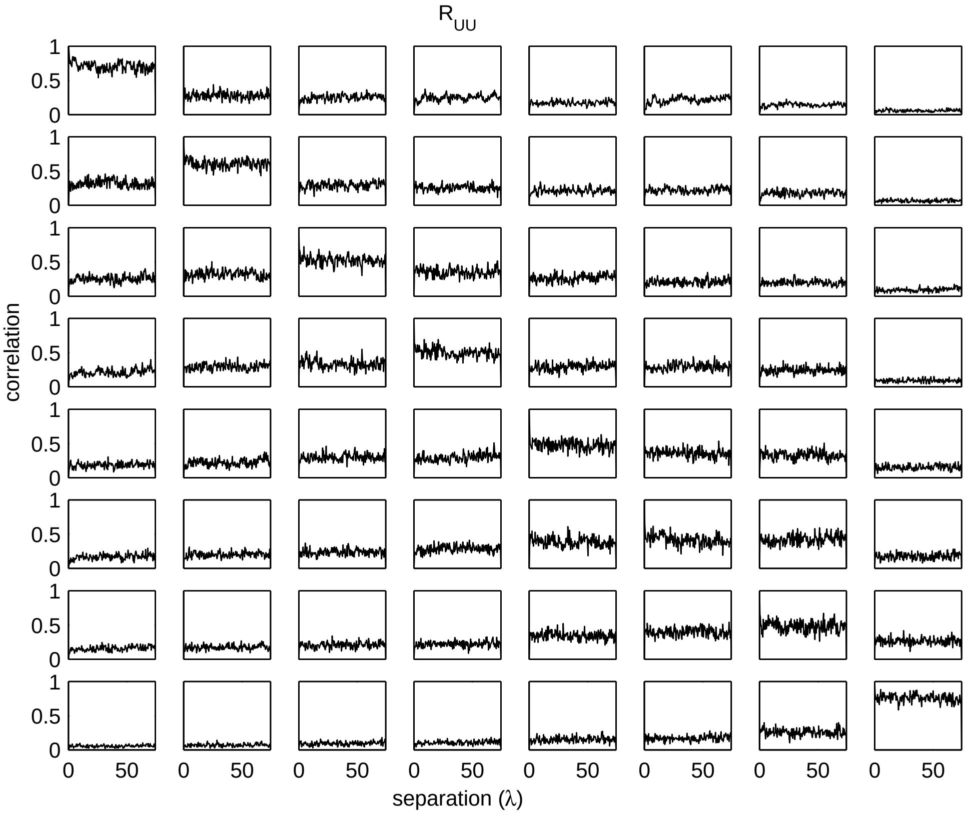

Figure 6.17: Alignment between left singular vectors. Experiment D, 8×8 MIMO.

corresponding to the two receivers are independent. $\mathbf{R_{UU}}$ for these experiments, however, showed higher correlation than the two ring model predicted.

Two outdoor measurement experiments conducted were representative of a sparse multipath environment in comparison to the indoor measurements. The correlation in the first few equal position singular vectors was measured to be very high, suggesting that a small number of dominant scatterers took role in the transmission. Eigenbeams computed from the left and right singular vectors were shown that reinforced this implication.

Chapter 7

Conclusion

7.1 Summary

This work demonstrates the possibility of MIMO wireless channel modeling based on an information-theoretic viewpoint. Correlation in the singular vectors was examined since the SVD is a widely used tool in MIMO transmission signal processing. For the multi-user downlink MIMO channel, correlation in the singular vectors of two users impacts the achievable capacity from SDMA transmission methods.

To model this correlation between singular vectors, the two ring MIMO model was used due to its natural extension to the multi-user case and its intuitiveness in understanding the formation of the singular vectors as the eigenbeams of the channel. Because the two ring model relies on a physical description of the location of scatterers and antenna arrays, it is also a good candidate for analyzing different paths and orientations taken by the transmitters and receivers. Furthermore, in Chapter 2 it was discussed how the two ring model can easily be cast into the framework of the successful SVA channel model. Many different Monte Carlo simulations were performed using the two ring model that were representative of the effect that different channel model assumptions have on the alignment of the singular vectors. The results of an i.i.d. complex Gaussian channel were given as a basis for independently aligned singular vectors.

Capacity simulations performed in Chapter 4 using the block-diagonalization algorithm showed the effect of singular vector alignment on achievable signalling rates. Two scalar metrics were used to analyze this effect in order to allow for a simple description of this effect. The BD algorithm is fairly robust in terms of singular vector correlation, except when the dominant singular vectors are very closely aligned. It is likely that the effect of singular vector correlation is greater when an available null space of the channel matrix for one user doesn't exist to accommodate SDMA modulation to the other user, as in the case where both receiving users have the same number of antennas as the transmitter. This is a likely scenario for ad-hoc networks or more complex broadcast and multiple access channels.

New hardware was designed and constructed as a multi-user extension to an existing MIMO measurement platform. Data collected using this hardware allowed for analysis of actual physical wireless channels. The results showed that alignment in singular vectors remains fairly constant over receiver separation distances on the order of a hundred wavelengths at carrier frequencies around 2.45 GHz. The two ring model scenario that matched this behavior employed separate scattering rings around each receiver. Outdoor measurements taken in a large field showed close singular vector alignment among dominant modes. This result corresponded well with a two ring model that used only a few scatterers in each ring.

7.2 Future Research

Following are suggestions for future work related to the research presented in this thesis:

1. The most obvious extensions of this work are to build more complexity into the two ring model to allow for more accurate modeling of the collected data results. In particular, the measurements showed higher correlation in $\mathbf{R_{UU}}$ than was portrayed in any of the two ring simulations. Deeper analysis of array types and orientations can be performed using the two ring model, as well as different path orientations. Perhaps locating the scatterers on the circumference of a ring doesn't accurately allow for modeling of singular vector correlation versus separation between receivers in a MIMO environment. However, changing this structure of the model imputes much more complexity into the model. Different

arrangements of the model that more accurately fit real data could be researched that retain simplicity. This tradeoff between model accuracy and simplicity is something that is balanced in virtually every model of physical phenomena.

2. Another natural extension to this research is to examine singular vector correlation through more measurement experiments of characteristicly different wireless channels. This research was limited to a study at a microwave carrier of roughly 2.45 GHz. Only two types of antenna arrays were used, the monopoles and dual polarized patch antennas. Other indoor and outdoor locations could be probed, such as a large gymnasium, a stadium, an urban environment, etc.

3. It would be very interesting to research the effects of alignment between the singular vectors of different users on capacity or near capacity achieving methods for multi-user scenarios with $N_R > N_T$, particularly where all arrays have the same number of elements. Singular vector correlation may have a greater effect to capacity in this latter case since each singular matrix provides a complete basis for complex N space, i.e., there doesn't exist a null space usable for modulation to other users. This direction of research may require implementing dirty-paper coding techniques, a difficult but useful endeavor.

4. Researching singular vector correlation and its effects was motivated by an information-theoretic standpoint. However, the metrics used in this paper were more ad-hoc than mathematically derived and were only shown to weakly effect the capacity of one algorithm. In other words, it is very likely that more telling metrics can be reasoned from a thorough examination of the underlying assumptions and factors influencing both theoretical capacity and achievable rates of different methods. Better models that more relevantly describe the MIMO channel from this viewpoint would be very powerful. Novel metrics with greater effect on capacity for multi-user MIMO networks can be more closely analyzed using these models.

Bibliography

[1] C. E. Shannon, "A Statistical Model of Urban Multipath Propagation", *Bell Systems Technical Journal*, vol. 27, pp. 379, 1948.

[2] G. J. Foschini and M. J. Gans, "On limits of wireless communications in a fading environment when using multiple antennas", *Wireless Personal Communications*, vol. 6, no. 3, pp. 311–335, March 1998.

[3] G. L. Turin, F. D. Clapp, T. L. Johnston, S. B. Fine, and D. Lavry, "A Statistical Model of Urban Multipath Propagation", *IEEE Trans. on Vehicular Technology*, vol. 21, no. 1, pp. 1–9, February 1972.

[4] K. I. Pedersen, P. E. Mogensen, and B. Fleury, "A Stochastic Model of the Temporal and Azimuthal Dispersion Seen at the Base Station in Outdoor Propagation Environments", *IEEE Trans. on Vehicular Technology*, vol. 49, no. 2, pp. 437–447, March 2000.

[5] A. A. M. Saleh and R. A. Valenzuela, "A Statistical Model for Indoor Multipath Propagation", *IEEE Journal on Selected Areas in Communications*, vol. SAC-5, no. 2, pp. 128–137, February 1987.

[6] Q. H. Spencer, B. D. Jeffs, M. A. Jensen, and A. Lee Swindlehurst, "Modeling the Statistical Time and Angle of Arrival Characteristics of an Indoor Multipath Channel", *IEEE Journal on Selected Areas in Communications*, vol. 18, no. 3, pp. 347–360, 2000.

[7] J. Wallace, *Modeling Electromagnetic Wave Propagation in Electrically Large Structures*, PhD thesis, Brigham Young Univerisity, Provo, UT, 2002.

[8] W. C. Jakes, *Microwave Mobile Communications*, IEEE Press, 1993.

[9] G. J. Foschini, "Layered Space-Time Architecture for Wireless Communication in a Fading Environment When Using Multi-Element Antennas", *Bell Labs Technical Journal*, vol. 1, no. 2, pp. 41–59, Autumn 1996.

[10] A. Lozano, F. R. Farrokhi, and R. A. Valenzuela, "Lifting the Limits on High-Speed Wireless Data Access Using Antenna Arrays", *IEEE Communications Magazine*, pp. 156–162, September 2001.

[11] Q. Spencer, A. Swindlehurst, and M. Haardt, "Zero-Forcing Methods for Downlink Spatial Multiplexing in Multi-User MIMO Channels", *IEEE Transactions on Signal Processing*, vol. 52, no. 2, February 2004.

[12] I. E. Teletar, "Capacity of Multi-antenna Gaussian Channels", *Euro. Trans. Telecom*, vol. 10, pp. 585–595, 1999.

[13] C. Peel, Q. Spencer, A. Lee Swindlehurst, and B. Hochwald, "Downlink Transmit Beamforming in Multi-User MIMO Systems", Submitted for publication, 2004.